Nearly homogeneous and isotropic turbulence generated by the interaction of supersonic jets

Takahiro Mori[1], Tomoaki Watanabe[2*], Koji Nagata[3]

[1] Department of Aerospace Engineering, Nagoya University, Nagoya, 464-8603, Aichi, Japan.

[2*] Education and Research Center for Flight Engineering, Nagoya University, Nagoya, 464-8603, Aichi, Japan.

[3] Department of Mechanical Engineering and Science, Kyoto University, Kyoto, 615-8530, Kyoto, Japan.

*Corresponding author(s). E-mail(s): watanabe.tomoaki@c.nagoya-u.jp;

Abstract

This study reports the development and characterization of a multiple-supersonic-jet wind tunnel designed to investigate the decay of nearly homogeneous and isotropic turbulence whose generation process is strongly influenced by fluid compressibility. The interaction of 36 supersonic jets generates turbulence that decays in the streamwise direction. The velocity field is measured with particle image velocimetry by seeding tracer particles with ethanol condensation. Various velocity statistics are evaluated to diagnose decaying turbulence generated by the supersonic jet interaction. The flow is initially inhomogeneous and anisotropic and possesses intermittent large-scale velocity fluctuations. The flow evolves into a statistically homogeneous and isotropic state as the mean velocity profile becomes uniform. In the nearly homogeneous and isotropic region, the ratio of root-mean-squared velocity fluctuations in the streamwise and vertical directions is about 1.08, the longitudinal integral scales are also similar in these directions, and the large-scale intermittency becomes insignificant. The turbulent kinetic energy per unit mass decays according to a power law with an exponent of about 2, larger than those reported for incompressible grid turbulence. The energy spectra in

[1]This version of the article has been accepted for publication in Experiments in Fluids, after peer review but is not the Version of Record and does not reflect post-acceptance improvements, or any corrections. Use of this Accepted Version is subject to the publisher's Accepted Manuscript terms of use https://www.springernature.com/gp/open-research/policies/accepted-manuscript-terms. The final version is available on https://doi.org/10.1007/s00348-024-03764-6.

the inertial subrange agree well with other turbulent flows when normalized by the turbulent kinetic energy dissipation rate and kinematic viscosity. The non-dimensional dissipation rate $\boldsymbol{C_\epsilon}$ is within a range of 0.56–0.87, which is also consistent with incompressible grid turbulence. The dependence of $\boldsymbol{C_\epsilon}$ on the turbulent Reynolds number aligns with the scaling of non-equilibrium turbulence, leading to the large decay exponent.

Keywords: Homogeneous isotropic turbulence, Jet interaction, Compressible turbulence

1 Introduction

Compressible turbulence plays a crucial role in flows in engineering and physics fields (Anderson, 1990; Canuto, 1997). For sufficiently large velocity fluctuations, turbulent motion begins to cause fluid compression and expansion, by which fluid density varies. The compressibility effects significantly alter the evolution of turbulence, as briefly introduced herein. Turbulent shear flows spatially grow by the momentum transport by turbulence. Their growth rates are known to be suppressed at a high Mach number (Bradshaw, 1977). When a Mach number defined for velocity fluctuations is very high, turbulent motion locally generates shock waves called shocklets, whose quasi-discontinuous jumps of flow variables influence turbulence (Lee et al, 1991). The decay of freely evolving turbulence in absence of mean shear has been extensively studied by experiments of grid turbulence generated in subsonic wind tunnels. The turbulent kinetic energy per unit mass, k_T, in grid turbulence is known to decay with a streamwise position x, according to a power law given by $k_T = a_k(x - x_0)^{-n}$, with a coefficient a_k, a virtual origin x_0, and a decay exponent n. Experiments of compressible grid turbulence in shock tubes and high-speed wind tunnels have observed the variations of x_0 and n due to compressibility effects. Another example of the compressibility effects is in the Reynolds number dependence of velocity derivative statistics. In fully-developed incompressible turbulence, the skewness and flatness of a longitudinal velocity gradient, e.g., $\partial u/\partial x$, have universal relations with a turbulent Reynolds

number (Sreenivasan and Antonia, 1997). Compressible turbulence tends to have larger absolute values of skewness and flatness than incompressible turbulence with a comparable Reynolds number, as confirmed by direct numerical simulations (DNS) of compressible isotropic turbulence (Donzis and John, 2020; Watanabe et al, 2021) and experiments of turbulence generated by the interaction of supersonic synthetic jets (Yamamoto et al, 2022a).

Theoretical studies of turbulence often consider homogeneous isotropic turbulence (HIT) (Batchelor, 1953), for which various theories and models have been developed in previous studies, e.g., non-dimensional energy dissipation rate (Lohse, 1994), longitudinal structure functions (Bos et al, 2012), and decay in the absence of external force (Davidson, 2009). Laboratory experiments are as crucial as numerical simulations in providing data that support the construction and validation of theories and models. Previous studies have developed various facilities and methods for generating HIT in a subsonic regime for which the assumption of incompressibility is valid. A grid installed in a uniform mean flow in a wind tunnel can generate nearly homogeneous and isotropic turbulence (e.g., Comte-Bellot and Corrsin 1966; Uberoi and Wallis 1967; Valente and Vassilicos 2011; Kitamura et al 2014; Djenidi et al 2015). Similarly, experiments with water flumes utilize a grid to generate HIT (Tan and Ling, 1963; Suzuki et al, 2010). Most grids consist of many intersecting bars, which stir a uniform mean flow. Another type of turbulence-generating grid is an active grid (Makita, 1991), which utilizes rotating bars with winglets. The random motion of winglets can generate HIT with a high Reynolds number (Mydlarski and Warhaft, 1996; Larssen and Devenport, 2011; Zheng et al, 2021b). A similar method to randomly stir fluid is utilized in a multi-fan wind tunnel, by which the interaction of fan-induced flows generates HIT (Ozono and Ikeda, 2018; Takamure and Ozono, 2019). A mean flow advects the HIT generated in wind tunnels and water flumes. Because of negligible shear in the mean flow, turbulence decays as it evolves in the streamwise direction.

Additionally, the interaction of multiple jets is also utilized to generate HIT, such as the interaction of synthetic jets (Hwang and Eaton, 2004; Variano et al, 2004) and randomly actuated jets (Bellani and Variano, 2014; Carter et al, 2016; Pérez-Alvarado et al, 2016). A turbulence-generating grid with a function of multiple jet injections from the grid bars has also been used in previous studies (Gad-el Hak and Corrsin, 1974; Tan et al, 2023).

Fewer experimental studies have been reported for HIT in compressible flows than in incompressible flows. Compressible grid turbulence has been investigated in shock tube facilities. Grid turbulence is generated when the mean flow induced by a planar shock wave passes a grid installed inside a shock tube. Most studies of grid turbulence in shock tubes focus on the interaction between the shock wave and grid turbulence (Honkan and Andreopoulos, 1992; Agui et al, 2005; Fukushima et al, 2021) while Briassulis et al (2001) have conducted detailed velocity measurements of grid turbulence. Zwart et al (1997) have reported the generation of grid turbulence with a perforated plate installed in a high-speed wind tunnel. Recent studies have developed other facilities for compressible turbulence. Yamamoto et al (2022b) developed a compressible-turbulence chamber with opposing arrays of piston-driven synthetic jet actuators. The piston-driven actuators, initially proposed by Crittenden and Glezer (2006), are capable of generating supersonic synthetic jets at a sufficiently high operation frequency (Traub et al, 2012; Sakakibara et al, 2018; Pham et al, 2023). The interaction of supersonic synthetic jets generates turbulence strongly influenced by compressibility effects. Another recently developed facility for compressible turbulence is the variable density and speed-of-sound vessel. The experiments use a heavy gas (sulfur hexafluoride SF_6) as a working fluid. Even though a stirring device generates a flow with a velocity lower than 100 m/s, the Mach number can be high because of the low speed of sound of SF_6. These new facilities will be helpful in the future investigation of compressible turbulence.

The compressibility effects on turbulence are not universal and may depend on various factors, including the generation process of turbulence. One of the critical parameters in compressible turbulence is the turbulent Mach number, defined as $M_T = \sqrt{u_{rms}^2 + v_{rms}^2 + w_{rms}^2}/a$, where u_{rms}, v_{rms}, and w_{rms} are the root-mean-squared (rms) velocity fluctuations in three directions, and a is the speed of sound. M_T is often treated as a dominant parameter determining compressibility effects (Lee et al, 1991; Ristorcelli and Blaisdell, 1997). However, a comparison of different compressible turbulent flows in experiments and direct numerical simulations (DNS) has shown that the compressibility effects on the velocity gradient statistics are not solely determined by local values of M_T (Yamamoto et al, 2022a): the deviation of the velocity derivative flatness from incompressible values occurs in supersonic turbulent jets and turbulence generated by supersonic synthetic jets at much lower M_T than in compressible HIT sustained by solenoidal forcing. Dilatational fluid motion causes additional kinetic energy dissipation in strongly compressible turbulence. The dilatational and solenoidal dissipation ratio is not also determined solely by M_T (Donzis and John, 2020). These behaviors are possibly explained by a non-local property of wave motion (Yamamoto et al, 2022a): even if a particular location in turbulence has low M_T, much higher values of M_T can be observed in other regions, where strong pressure waves, such as shock waves, are generated and propagate into a flow region of interest. Similarly, the compressibility effects on the decay of grid turbulence are also different among experiments. The experiments of grid turbulence in a shock tube by Briassulis et al (2001) suggest that compressibility effects cause the decrease of n in the power law for the turbulent kinetic energy decay, $k_T = a_k(x - x_0)^{-n}$. Later, Fukushima et al (2021) also observed the decrease of n in compressible grid turbulence in their shock tube. However, Zwart et al (1997) reported that n in grid turbulence in a high-speed wind tunnel exceeds values in incompressible cases when the mean flow Mach number is high. Zwart et al (1997) also observed that n becomes small when the

Mach number is moderately large. These grid turbulence experiments were conducted for low-M_T conditions in the decay region. These results imply that the compressibility effects on grid turbulence are not universal and may depend on various factors, including the generation process of turbulence, as also discussed in Zwart et al (1997). Indeed, even in an incompressible fluid, different decay laws of HIT were theoretically derived for the decay of Saffman turbulence and Batchelor turbulence, which differ in the shape of an energy spectrum at a low wavenumber range (Davidson, 2004). The low-wavenumber spectral shape depends on the turbulence generation process. Therefore, different compressibility effects are possible for the decay of HIT generated in different facilities.

These studies imply that the compressibility effects on turbulence significantly depend on the generation process of turbulence. Investigating compressible turbulence in various facilities is crucial in extending our knowledge of turbulence behavior under compressibility effects. The further development of compressible turbulence facilities is demanded for this purpose. The present study develops a new wind tunnel facility to investigate compressible decaying HIT. In this wind tunnel, the interaction of many supersonic jets generates nearly homogeneous and isotropic turbulence, which continuously decays in a test section without significant influences of mean shear. This paper characterizes the turbulent flow generated in the multiple-supersonic-jet wind tunnel with velocity measurements with particle image velocimetry (PIV), temperature and pressure measurements, and Schlieren visualization. The paper is organized as follows. Section 2 describes the multiple-supersonic-jet wind tunnel and measurement methods. Section 3 presents the measurement results to discuss the fundamental turbulence statistics compared with other turbulent flows. Finally, the paper is summarized in Sect. 4.

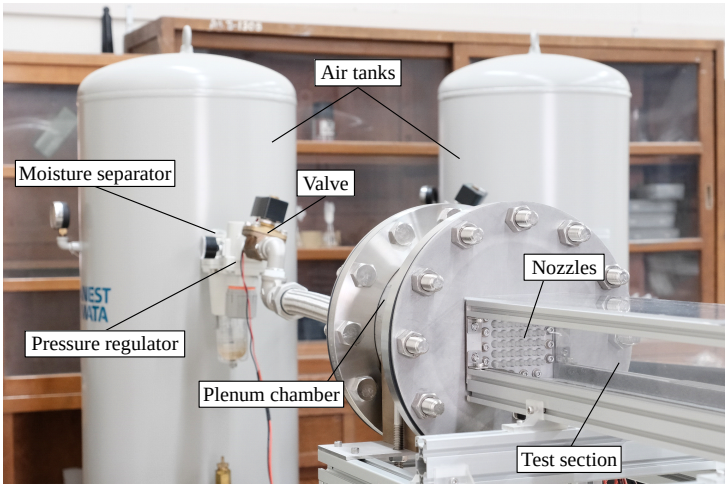

Fig. 1 A multiple-supersonic-jet wind tunnel.

2 Experimental setup and measurement methods

2.1 Multiple-supersonic-jet wind tunnel

The multiple-supersonic-jet wind tunnel generates nearly homogeneous and isotropic turbulence by the interaction of supersonic round jets. The development of the facility is motivated by the experiments of incompressible HIT generated by the interaction of many subsonic jets (Gad-el Hak and Corrsin, 1974; Carter et al, 2016; Tan et al, 2023). Figure 1 shows a picture of the wind tunnel with three main components: an air supply system, a plenum chamber, and a test section. Compressed air is supplied to the cylinder-shaped plenum chamber. The front surface of the plenum chamber is equipped with 36 Laval nozzles, which generate supersonic round jets. The interaction of 36 jets generates turbulence which eventually decays in the streamwise direction in the test section. The wind tunnel is specifically designed to investigate the impact of compressibility effects during the turbulence generation process on the decay of turbulence. The generation process is fully influenced by fluid compressibility via the interaction of supersonic jets. In the decay region, local compressibility effects are

expected to be minimal, as confirmed by velocity measurements. This section describes the details of the wind tunnel.

The concept of homogeneity pertains to the uniform distribution of all velocity statistics across a cross-section at a fixed streamwise location. Additionally, it involves the mean velocity distribution being uniform in both streamwise and cross-sectional directions. Isotropy concerns the statistics of velocity fluctuations, and the statistics of the three fluctuating components of the velocity vectors are identical if the flow is statistically isotropic. In contrast, the mean velocity vector has a non-zero value only in the mean flow direction. The statistical homogeneity and isotropy of turbulence generated by the supersonic jet interaction are examined with various velocity statistics in this study.

Compressed air is stored in two air tanks with a volume of 220 L (Anest Iwata, SAT-220C-140). Compressors (Fujiwara Industrial Co., Ltd., SW-L30LPF-01) are connected to each tank via a moisture separator (SMC, AFM40-02-2A). The outlet port of each tank is connected to the back surface of the cylinder-shaped plenum chamber by a flexible hose with an inner diameter of 29.5 mm. Here, the air is supplied to the chamber through a moisture separator (SMC, AF60-10-A), a pressure regulator (SMC, AR60-10BG-B), and a pilot kick 2-port solenoid valve (CKD, ADK11-25A). The pressure regulator is used to adjust the plenum pressure.

Figure 2 shows a schematic of the plenum chamber and test section. The plenum chamber consists of a 180 mm length pipe and two round plates with a 330 mm diameter fixed on flanges welded to the pipe. The pipe size is JIS 20A, with an inner diameter of 206.3 mm and a thickness of 5 mm. The pipe, plates, and flanges are made of stainless steel. Rubber seals designed for JIS 20A pipes fill the space between the plates and flanges. The flexible hoses are connected to two threaded holes on the back plate with a thickness of 6 mm. A pressure sensor (SMC, ISE30A-C6L-N-M) connected to a port on the front plate monitors the pressure in the plenum chamber. The plenum

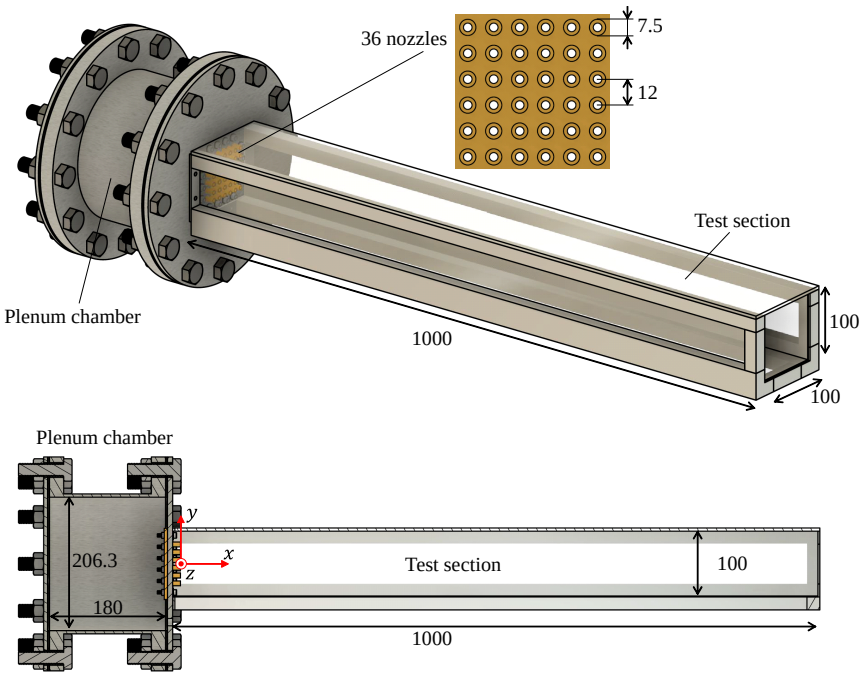

Fig. 2 A schematic of the multiple-supersonic-jet wind tunnel. All dimensions are in mm.

pressure is also measured with another pressure sensor (SMC, PSE-540A R06), whose signal is recorded by an oscilloscope (Yokokawa, DL850E) at a sampling rate of 1 kHz.

A nozzle plate with 6×6 Laval nozzles is installed on the front plate. Figure 3(a) shows a picture of the nozzle plate manufactured with stereolithography 3D printing with a printing resolution of 10 μm. All 36 nozzles have the same geometry. The holes along the perimeter of the nozzle plate are used to fix the plate to the plenum chamber. The inner diameters at the jet exit and the throat are 4.31 mm and 4.12 mm, respectively. The nozzle inlet diameter is 6.3 mm. The constant outer diameter is 7.5 mm. The center-to-center distance between the two nozzles is 12 mm. The inner diameter of the converging section varies according to the square of a sinusoidal function. The internal geometry of the diverging section is determined with an analytical method for nozzle design (Foelsch, 1949). Each nozzle with these dimensions generates a fully expanded supersonic jet with a Mach number of 1.36 in atmospheric air when

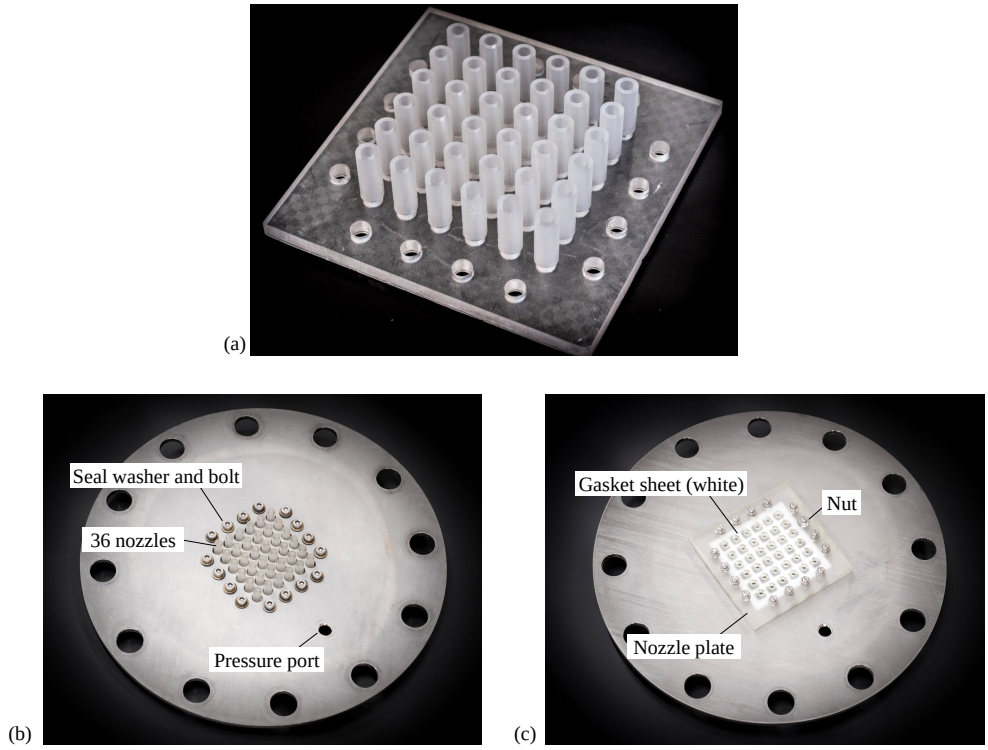

Fig. 3 (a) A nozzle plate with 36 Laval nozzles. The nozzle plate installed on the front plate of the plenum chamber: (b) outer side and (c) inner side.

the gauge pressure in the chamber is 200 kPaG. The flow within the nozzle becomes choked for the plenum pressure exceeding 38.8 kPaG. The nozzle produces a supersonic flow with the constant Mach number when the plenum pressure surpasses 51.2 kPaG. Any further increase in plenum pressure beyond 51.2 kPaG does not change the Mach number. The base of the nozzle plate has a square shape of 110×110 mm^2 and a thickness of 5 mm. The front plate of the chamber has holes with a diameter of 9 mm at the locations corresponding to the nozzles, as shown in Fig. 3(b). The nozzles are inserted and fixed from the inner side of the chamber plate with bolts and nuts [Fig. 3(c)]. Air leakage is prevented with seal washers used with the nuts and a hand-cut PTFE gasket sheet with a 1 mm thickness, which fills the space between the nozzle plate and the chamber plate. The nozzle plate is supported by the inner surface

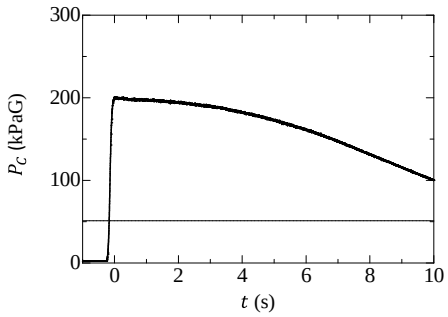

Fig. 4 Temporal variation of gauge pressure in the plenum chamber, P_C. $t = 0$ corresponds to the maximum value of P_C. The horizontal line indicates 51.2 kPaG, above which the jet Mach number $M_J = 1.36$ does not depend on P_C.

of the chamber plate, preventing damage to the nozzle plate due to pressure forces. Additionally, visualization experiments are conducted for a supersonic jet generated by a single nozzle. The internal nozzle geometry is the same as for the multi-nozzle plate, but the single-nozzle plate has one nozzle at the center of the plate. The outer diameter of the nozzle is 8 mm. The single-nozzle plate is also mounted on another front plate of the plenum chamber, which has a hole at the center corresponding to the nozzle position.

The test section has 100×100 mm^2 square cross-section and 1000 mm length. The test section is made of an aluminum frame and acrylic plates. For the side and bottom walls, optical-grade acrylic sheets (Nitto Jushi Kogyo, CLAREX) with a 1.5 mm thickness are used for optical measurements and visualizations. The top wall is a conventional acrylic plate with a 3 mm thickness. The plenum chamber is placed on a urethane pipe-holder designed for JIS 20A pipes (Nichiei Intec, N-040219). The test section and pipe holder are fixed on another aluminum frame.

All experiments are conducted to generate the supersonic jets with a plenum pressure of 200 kPaG. The streamwise, vertical, and spanwise directions are denoted by x, y, and z, respectively, and the origin of the coordinate system is at the center of the jet exits of the nozzle plate, as shown in Fig. 2. In each run of the experiments, the air tanks are filled with compressed air with a gauge pressure of 900 kPaG. Once

the valves are opened, the compressed air flows into the plenum chamber, increasing the plenum pressure. The pressure regulators between the air tanks and the plenum chamber are adjusted to realize the desired value of the plenum pressure. Figure 4 presents the temporal variation of the gauge pressure in the plenum chamber, P_C, during the experiment. In this plot, $t = 0$ corresponds to the maximum value of P_C. After the valve is opened, the pressure immediately increases to 200 kPaG. The pressure hardly varies with time for about 3 s, and then begins to decrease because the pressure in the air tanks decreases. The plenum pressure decreases from 200 kPaG by 5% at $t = 2.9$ s. The flow in the test section is statistically steady for about 2 s, for which the measurements are conducted in this study. As long as the plenum pressure is greater than 51.2 kPaG shown by the horizontal line, the jet Mach number is not sensitive to the pressure.

2.2 Particle image velocimetry

Velocity measurements are conducted with two-dimensional and two-component PIV. The present study uses the DANTEC PIV system, which consists of a double-pulse Nd:YAG laser (Dantec Dynamics, Dual Power 65-15) and a high-speed camera (Dantec Dynamics, SpeedSense 9070, 1280×800 pixels) with a camera lens with a focal length of 105 mm (Nikkon, AI AF Micro Nikkor 105mm F2.8D). The system is controlled with a synchronizer (Dantec Dynamics, 80N77) and PIV software (Dantec Dynamics, Dynamic Studio). Light sheet optics mounted on the laser produce a thin light sheet with a thickness smaller than 1 mm. The laser unit is placed under the wind tunnel, and a mirror in front of the laser sheet optics is used to illuminate an x–y plane from the bottom of the test section. The camera captures particle images from the side of the test section. The time interval of two laser pulses is adjusted depending on the measurement location, as discussed below. Each laser pulse has a width of less than 4 ns. The particle-pair images are captured at 15 Hz. The images

are processed with an adaptive PIV algorithm (Theunissen, 2010) and universal outlier detection (Westerweel and Scarano, 2005) implemented in Dynamic Studio. In the adaptive PIV algorithm, the minimum and maximum interrogation area grids are set as 16×16 and 32×32, respectively.

The present PIV uses condensed ethanol droplets generated by the Laval nozzles as tracer particles. Liquid ethanol is seeded and evaporated in the air tanks before the experiments. When fluid with evaporated ethanol passes the Laval nozzles, fluid expansion in the diverging sections causes a temperature drop, resulting in the condensation of ethanol. This seeding technique has widely been used in supersonic wind tunnels, which also use divergent nozzles to produce supersonic flows. Previous studies have confirmed that generated particles have diameters less than 1 μm: Pizzaia and Rossmann (2018) reported that the diameter of ethanol droplets was approximately 0.05–0.2 μm; Kouchi et al (2019) used acetone droplets produced by a Laval nozzle for PIV measurement, by which the droplet diameter was estimated as 160 nm. These studies have shown that the condensation droplets are small enough for PIV measurements of supersonic flows. The diameter can be estimated from light scattered by droplets. By visibly observing particles illuminated by white LED (Sigmakoki, SLA-100A), the droplet diameter is confirmed to be in the Rayleigh-scattering regime and smaller than visible light wavelength, 360–830 nm. The present study investigates turbulence generated by the interaction of supersonic jets. As the jets mix with ambient fluid, the mean velocity in the measurement area is in a subsonic regime. For the present velocity range, the ethanol droplets are useful as tracer particles of PIV. Kouchi et al (2019) have previously verified that PIV using tracer particles formed by acetone condensation can capture a distinct velocity jump across a shock wave. While our current study does not aim to investigate supersonic flows near the nozzles, the use of condensation droplets as tracers is a promising technique for PIV of high-speed flows.

Table 1 Locations and parameters of PIV measurements.

x_C	0.150 m	0.267 m	0.360 m	0.465 m	0.605 m	0.746 m
y_C	0 m	0 m	0 m	0 m	0 m	0 m
Δt	3 μs	4 μs	4 μs	4 μs	4 μs	4 μs
N_S	722	797	700	726	651	595

Because how the ethanol is injected in the air tanks affects the number density of tracer particles in the test section, we describe the detailed procedure of the experiments. The air tanks have three ports: an inlet port connected to the compressor, an outlet port connected to the plenum chamber, and an exhaust port used to release compressed air after experiments. The exhaust port can be opened or closed by a hand-operated valve, while the inlet port can be opened by disconnecting a gas hose from the compressor. The following procedure is repeated for the two air tanks. First, ethanol is sprayed into the air tank via the inlet port by using an airbrush. Sprayed ethanol quickly evaporates in the tank. When ethanol is injected, the exhaust valve is kept partially opened to prevent the reversal flow from the inlet port. 70 ml of liquid ethanol is injected into each tank. The exact amount of ethanol in the tank is difficult to estimate because the air partially leaks from the tank while spraying the ethanol. However, we have confirmed that increasing the amount from 70 ml does not influence particle images captured by the PIV system, whereas smaller amounts result in fewer particles. After the compressor is connected to the inlet port of the tank again and the exhaust valve is closed, the air is stored in the tank until the gauge pressure reaches 900 kPaG. Even for a supersaturated case, the mass fraction of ethanol at this stage is smaller than 1%, for which the ethanol/air mixture and condensation are expected to have negligible influences on the turbulent flow in the test section (Clemens and Mungal, 1991; Pizzaia and Rossmann, 2018). We have also confirmed that ethanol does not change the average and standard deviation of dynamic pressure measured with a Pitot tube.

Upon operating the valves, starting jets form in the test section. The PIV measurements are conducted after these starting jets have completely passed through the measurement location. The camera starts to capture particle-image pairs prior to valve activation. Before the turbulence fully develops, the camera records images with few particles. The tracer particles are produced through the fluid expansion occurring in the supersonic flow within the Laval nozzle. Therefore, the camera captures images with fewer particles during the transitional phase with the starting jets compared to the fully-developed turbulence phase. Typically, these images are collected for around 0.2 s (equivalent to the first two or three images with particles) and are not used in the analysis. When the flow reaches full development, the images become densely populated with particles emitted by the nozzles, signaling the commencement of the PIV measurement. Through this method, we effectively exclude the transitional phase of the starting jets from the PIV measurements. Velocity vectors are calculated by analyzing the images captured while the plenum pressure is constant.

The PIV measurements are conducted at six streamwise locations. Table 1 summarizes the measurement locations and parameters. The center of the measurement area is $(x, y) = (x_C, y_C)$. These locations are chosen to investigate turbulence generated by the jet interaction and do not include the region where each jet evolves before the interaction. This is because our primary interest is in a nearly homogeneous and isotropic region where turbulence decays. Although the supersonic jets are issued in the test section, the mean velocity in the measurement locations is subsonic because the high-speed jets mix with surrounding fluids with a small mean velocity. The table also shows the time interval Δt between two pulses of the PIV. At $x_C = 0.150$ m, the flow is highly inhomogeneous in the cross-section, and the mean velocity along the centerline is higher than the surroundings. Therefore, Δt is smaller at $x_C = 0.150$ m than in the downstream region. These Δt values are determined based on the particle displacement during Δt. The measurement area is a rectangle, approximately 70 mm

in the streamwise direction and 40 mm in the vertical direction. Velocity vectors near the periphery of particle images are excluded from statistical analyses, as particles might enter or exit the image frames during the interval Δt. The spatial resolution, defined as the spacing between points to calculate velocity vectors, is about 1 mm in both directions. As shown below, the present PIV resolves the scales close to the small-scale end of the inertial subrange and does not resolve the smallest scale of turbulent motion. This resolution is sufficient to evaluate most velocity statistics dominated by large-scale motion. In each wind tunnel operation, about 35 snapshots of velocity vectors are captured on average. The experiments are repeated many times for statistical analysis. The total number of acquired vector images, N_S, is also shown in Table 1. The snapshots of velocity vectors are measured at 15 Hz, for which the time interval between two snapshots is 0.067 s. The mean velocity in the fully developed turbulent region is about 40 m/s. The characteristic length scale of the flow is roughly estimated as the spacing between the nozzles, 0.012 m. The flow time scale defined with these velocity and length scales is 0.0003 s, much shorter than the sampling interval. Thus, the snapshots of velocity vectors are independent samples that are not correlated with each other. Statistics are evaluated with ensemble averages. Two-dimensional velocity vectors are denoted by (u, v). For a variable f, the nth snapshot is denoted by $f^{(n)}(x, y)$. The average of f, $\langle f \rangle$, is evaluated as

$$\langle f \rangle(x, y) = \frac{1}{N_S} \sum_{n=1}^{N_S} f^{(n)}(x, y). \tag{1}$$

Fluctuations are defined as $f'^{(n)}(x, y) = f^{(n)}(x, y) - \langle f \rangle(x, y)$, and the rms fluctuations are evaluated as $f_{rms}(x, y) = \langle f'^2 \rangle^{1/2} = (\langle f^2 \rangle - \langle f \rangle^2)^{1/2}$. In addition, skewness and flatness of f are defined as $S(f) = \langle f'^3 \rangle / \langle f'^2 \rangle^{3/2}$ and $F(f) = \langle f'^4 \rangle / \langle f'^2 \rangle^2$, respectively.

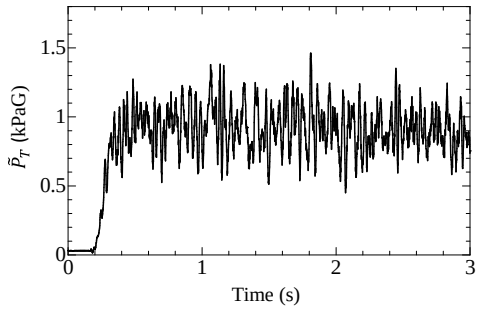

Fig. 5 Temporal variation of the total pressure $\tilde{P}_T$ measured at $x = 0.59$ m on the centerline of the test section. The signal is low-pass filtered by taking a local time average with a window size of 0.1 s.

2.3 Pitot tube measurement

Pitot tube measurements along the centerline of the test section are conducted to validate the PIV data. The present study uses an L-shaped standard Pitot tube with a 7 mm diameter (Testo, 0635 2145) and a pressure sensor (SMC, PSE543A-R06). The signal from the pressure sensor is recorded with an oscilloscope (Yokokawa, DL850E) at a sampling rate of 10 kHz. Total pressure P_T is measured at the tip of the tube, while static pressure P_S is measured on the side of the tube, which is separated from the tip by 30 mm in the streamwise direction. The top wall of the test section is replaced with many small plates between which the Pitot tube is inserted into the test section. The measurement location is along the centerline of the test section. As shown in Sect. 3.3, the streamwise distribution of static pressure $P_S(x)$ is well fitted by an exponential curve $P_{S,F}(x) = a_P(b_P)^x$, where the parameters can be obtained with a least squares method for measured P_S. Because the Pitot tube measures $P_T(x)$ and $P_{S,F}(x+\Delta_{Pitot})$ with $\Delta_{Pitot} = 30$ mm, the pressure difference $\Delta P(x) = P_T(x) - P_S(x)$ is calculated with the measured $P_T(x)$ and the fitting curve $P_{S,F}(x)$. A time average is calculated for the time series pressure data over 2 s, for which the plenum pressure is almost constant. Figure 5 displays the temporal variation of the instantaneous total pressure $\tilde{P}_T(t)$ measured at $x = 0.59$ m on the centerline of the test section. The time of 0 s denotes the start of the data recording process. When the valves are activated, $\tilde{P}_T$

rapidly increases while its fluctuations are attributable to turbulence. The initial rise of $\tilde{P}_T$ occurs over approximately 0.2 s, which is also close to the time of the supersonic jet formation, discussed below. Consequently, the present Pitot tube measurement system is capable of measuring the time-averaged dynamic pressure over a few seconds.

Because the measurements are conducted in turbulence, the velocity fluctuations also affect ΔP, whose measured values are not related solely to the dynamic pressure due to the mean flow. Turbulence increases the total pressure measured by the Pitot tube. The following relation expresses the pressure difference measured by a Pitot tube in turbulence (Bailey et al, 2013):

$$\Delta P = \frac{1}{2}\rho\left(\langle u\rangle^2 + \langle u'^2\rangle + \langle v'^2\rangle + \langle w'^2\rangle\right). \tag{2}$$

The velocity variances are evaluated with the PIV as $\langle u'^2\rangle + \langle v'^2\rangle + \langle w'^2\rangle \approx \langle u'^2\rangle + 2\langle v'^2\rangle$. Here, the Pitot tube measurement is conducted along the centerline, where $\langle v'^2\rangle \approx \langle w'^2\rangle$ is expected to be valid. The density is also estimated from static pressure and temperature measurements, as described below. Thus, the mean velocity is calculated from ΔP measured by the Pitot tube as

$$\langle u\rangle = \sqrt{\frac{2\Delta P}{\rho} - (\langle u'^2\rangle + 2\langle v'^2\rangle)}. \tag{3}$$

Equation (3) is used to assess the accuracy of PIV, specifically regarding mean velocity and velocity variances.

Another factor that may affect the Pitot tube measurement is the compressibility effect. However, based on the mean velocity measured with PIV, we have estimated that this effect results in underestimating the mean velocity only by less than 2%. Therefore, the compressibility correction for mean velocity is not applied to the Pitot tube measurement.

2.4 Temperature measurement

Temperature is measured with a fine sheathed K-type thermocouple (J Thermo, TJK-LS1501GP), whose sheath has a 0.15 mm diameter and a 100 mm length. The response time of this thermocouple is less than 1 s. The output voltage of the thermocouple is processed and recorded by a data logger (Hioki, LR8431) at a sampling rate of 100 Hz. Because of the response time, the temperature recorded over 1 s after 1 s from the start of the wind tunnel is averaged to estimate the mean temperature. The thermocouple is inserted from the top of the test section in the same manner as the Pitot tube. Temperature measurements are conducted at different streamwise locations.

2.5 Schlieren visualization

The supersonic jets generated by the 3D-printed nozzles are visualized using the Schlieren technique. The present study employs a Schlieren system manufactured by Kato Koken (System Schlieren, SS50III-L5). This system comprises a 5W LED light source, lens units for generating and collecting parallel light with a diameter of 50 mm, and a knife edge. Detailed information about the system can be found in Ishida et al (2023). The images are captured by a high-speed camera (Kato Koken, k5), capable of recording at a maximum frame rate of 8000 fps with a resolution of 640×480 pixels. This camera is paired with a C-mount lens featuring a focal length of 100 mm (Omron, 3Z4S-LE SV-10028H). The Schlieren visualization is performed without the test section because the acrylic walls of the test section distort the parallel light. The parallel light traverses the flow in the z direction. The knife edge is aligned perpendicularly to the flow, parallel to the vertical (y) direction, to effectively visualize the density gradient in the streamwise direction. The visualization experiments are also conducted for the single-nozzle plate to estimate the jet Mach number.

2.6 Estimation of the dissipation rate of turbulent kinetic energy

The decay of turbulent kinetic energy along the centerline is investigated for a nearly homogeneous and isotropic region corresponding to the downstream region. The turbulent kinetic energy per unit mass, $k_T = (\langle u'^2 \rangle + \langle v'^2 \rangle + \langle w'^2 \rangle)/2$ is evaluated as $(\langle u'^2 \rangle + 2\langle v'^2 \rangle)/2$ with the PIV data. The governing equation for k_T can be derived from the conservation equation of momentum for a compressible fluid, which is rewritten in the form of

$$\frac{\partial u_i}{\partial t} + u_j \frac{\partial u_i}{\partial x_j} = -\frac{1}{\rho}\frac{\partial p}{\partial x_i} + \frac{1}{\rho}\frac{\partial \tau_{ij}}{\partial x_j}. \tag{4}$$

Here, $p(x, y, z, t)$ and $\rho(x, y, z, t)$ are local values of pressure and density, respectively, and τ_{ij} is the viscous stress tensor. Multiplying Eq. (4) by $u_i' = u_i - \langle u_i \rangle$, taking an avereage, and rearranging terms yield the following governing equation for k_T:

$$\begin{aligned} \frac{\partial k_T}{\partial t} + \langle u_j \rangle \frac{\partial k_T}{\partial x_j} = & \underbrace{-\langle u_i' u_j' \rangle \frac{\partial \langle u_i \rangle}{\partial x_j}}_{P_k} \underbrace{-\frac{1}{2}\frac{\partial \langle u_i' u_i' u_j' \rangle}{\partial x_j}}_{D_T} + \underbrace{\left\langle \frac{u_i' u_i'}{2} \frac{\partial u_j'}{\partial x_j} \right\rangle}_{\Theta_k} \\ & \underbrace{-\left\langle \frac{1}{\rho}\frac{\partial u_j' p}{\partial x_j} \right\rangle}_{D_P} + \underbrace{\left\langle \frac{p}{\rho}\frac{\partial u_j'}{\partial x_j} \right\rangle}_{\Theta_P} + \underbrace{\left\langle \frac{1}{\rho}\frac{\partial u_i' \tau_{ij}}{\partial x_j} \right\rangle}_{D_V} - \underbrace{\left\langle \frac{\tau_{ij}}{\rho}\frac{\partial u_i'}{\partial x_j} \right\rangle}_{\varepsilon}. \end{aligned} \tag{5}$$

The first and second terms of the left-hand side represent the temporal variation of k_T and the advection due to mean flow, respectively. On the right-hand side, P_k is the production term, D_T is the turbulent diffusion term, D_P is the pressure diffusion term, D_V is the viscous diffusion term, and ε is the dissipation term. These terms also appear in the governing equation for an incompressible fluid. The remaining terms represent direct influences of fluid compressibility: Θ_k is the change in the turbulent kinetic energy per unit mass due to fluid expansion or compression, and Θ_P is the energy

conversion between the kinetic and internal energies by pressure work. These two terms arise from the advection and pressure terms in Eq. (4) because of $\partial u_i/\partial x_i \neq 0$ when the turbulent and pressure diffusion terms are derived. Even though the interaction of the supersonic jets generates turbulence near the nozzles, the velocity fluctuations in the decay region are subsonic, implying that Θ_k and Θ_P are not dominant in the variation of k_T. As long as the Reynolds number is not too small, the viscous contribution to the spatial transport of kinetic energy is negligible, and D_V is much smaller than other terms in turbulence (Watanabe et al, 2016; Wang et al, 2022). In addition, the flow is assumed to be statistically homogeneous in the y and z directions, and the diffusion terms in these directions are negligible. The turbulent and pressure diffusions in the streamwise direction are also negligible compared with the transport due to the mean flow in decaying HIT (Wang et al, 2022). Finally, the production term is also smaller than the remaining terms once the mean velocity distribution becomes uniform in the downstream region. Then, Eq. (5) is simplified as

$$\langle u \rangle \frac{\partial k_T}{\partial x} = -\varepsilon. \tag{6}$$

This relation is often used to evaluate the dissipation rate in grid turbulence because $\langle u \rangle$ and k_T are much easier to measure than ε (Kistler and Vrebalovich, 1966; Thormann and Meneveau, 2014). The decay of HIT depends on the spectral shape at large scales, which can differ depending on how turbulence is generated (Davidson, 2004). The compressibility effect on the decay properties may also emerge through the generation process of turbulence, although this influence does not appear in the governing equation of k_T. Such influences may appear in the virtual origin and decay exponent in the power law decay of k_T (Briassulis et al, 2001; Zwart et al, 1997).

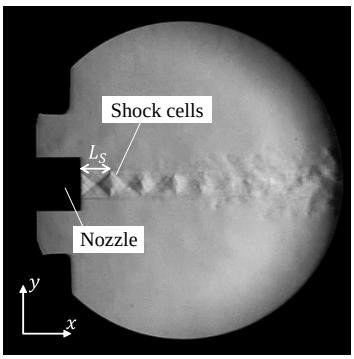

Fig. 6 Schlieren visualization of a supersonic jet generated by the single nozzle. The image is captured with the high-speed camera at 2000 fps and an exposure time of 1/150000 s.

Equation (6) is used to estimate the turbulent kinetic energy dissipation rate from the PIV data. The decay of k_T in HIT is well represented by a power law given by

$$k_T = a_k(x - x_0)^{-n}, \tag{7}$$

where a_k is a coefficient related to the level of velocity fluctuations, x_0 is the virtual origin, and n is the decay exponent (Mohamed and Larue, 1990; Davidson, 2004). A least squares method is applied to the streamwise distribution of k_T obtained by the PIV data. Then, ε is evaluated as

$$\varepsilon = \langle u \rangle a_k n (x - x_0)^{-n-1}. \tag{8}$$

3 Results and discussion

3.1 Instantaneous flow fields

Figure 6 presents Schlieren visualization of a supersonic jet generated by a single nozzle. A nearly ideally expanded supersonic jet typically forms periodic shock-cell

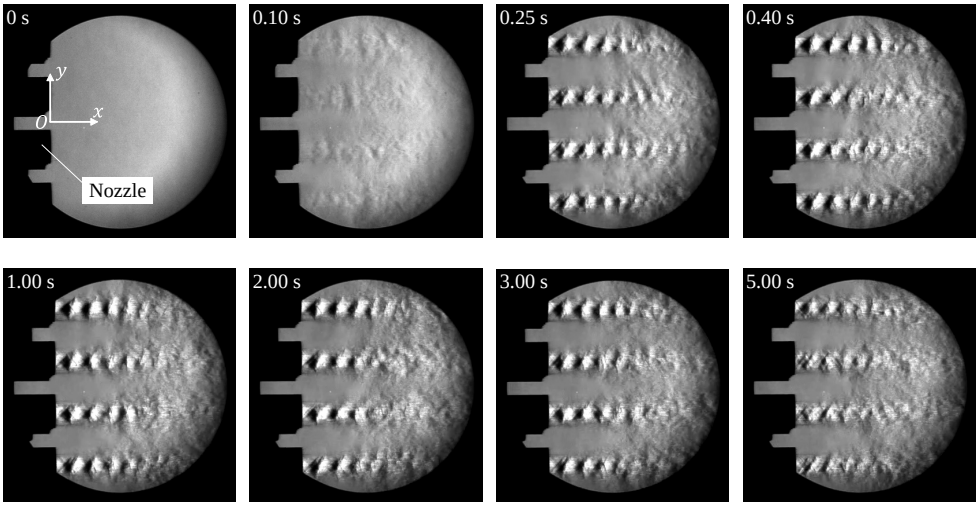

Fig. 7 Schlieren visualization of the interaction of supersonic jets generated by 36 nozzles. The images are captured with the high-speed camera at 500 fps and an exposure time of 1/150000 s.

structures near the nozzle exit (Tam, 1972). The Schlieren image also displays these shock cells. The location of the shock cells does not vary with time once the jet has fully developed. The length of the shock cell, L_S, is associated with the jet Mach number, M_J, as per Prandtl's formula (Pack, 1950; Tam, 1972):

$$\frac{L_S}{d} = \frac{\pi}{\beta}\sqrt{M_J^2 - 1}, \tag{9}$$

where $\beta = 2.405$ and d is the diameter of the nozzle exit. The length of the first shock cell is estimated to be $L_S = 5.0$ mm. The above equation with $L_S = 5.0$ mm and $d = 4.31$ mm yields $M_J = 1.33$, aligning closely with the design Mach number. Furthermore, the nearly constant jet width near the nozzle suggests that the jet-to-ambient pressure ratio is about 1.

Figure 7 presents the visualization for the multi-nozzle case. Time is indicated at the top left of each panel and ranges from 0 s to 5 s. Here, 0 s corresponds to the time at which the jet begins to appear in images upon opening the valves. The supersonic jets with the shock cells have fully developed by 0.25 s. Later, the flow feature, such

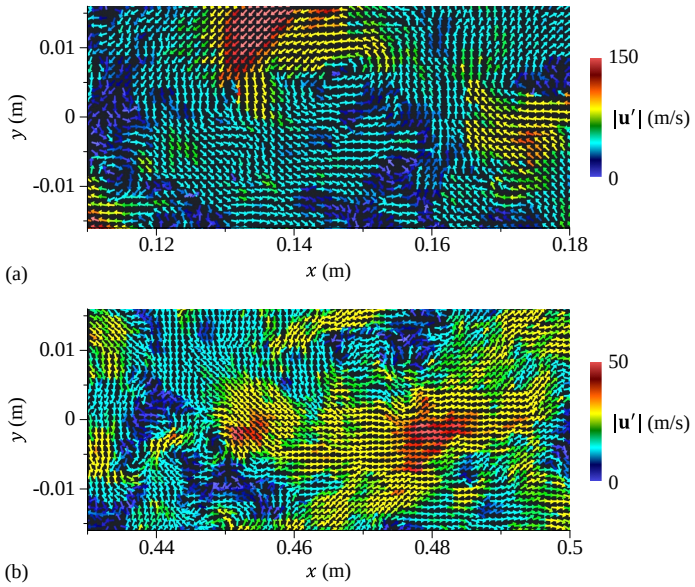

Fig. 8 Instantaneous fluctuating velocity vectors $\mathbf{u}' = (u', v')$ measured at (a) $x_C = 0.150$ m and (b) $x_C = 0.465$ m. The color represents the vector magnitude $|\mathbf{u}'|$.

as the location of the shock cells, does not vary with time, even at 3.0 s. For about 3 s, the wind tunnel is expected to sustain the statistically steady flow generated by the jet interaction. The shock-cell patterns are less clear in the last image at 5 s, relating to the temporal decrease in the plenum pressure.

Figure 8 shows instantaneous fluctuating velocity vectors $\mathbf{u}' = (u', v')$ measured at $x_C = 0.150$ m and 0.465 m. The color represents the vector magnitude. For both measurement locations, the turbulent jets from the nozzles have fully developed and have interacted with each other, and the clear imprints of each jet are not observed in the velocity field. At $x_C = 0.150$ m, the velocity fluctuations reach about 150 m/s. As turbulence decays, velocity fluctuations become small from $x_C = 0.150$ m to 0.465 m. At both locations, the vector fields exhibit typical rotating patterns associated with vortices, e.g., $(x, y) = (0.11$ m, -0.01 m) in Fig. 8(a), indicating that the present PIV well captures these turbulent structures.

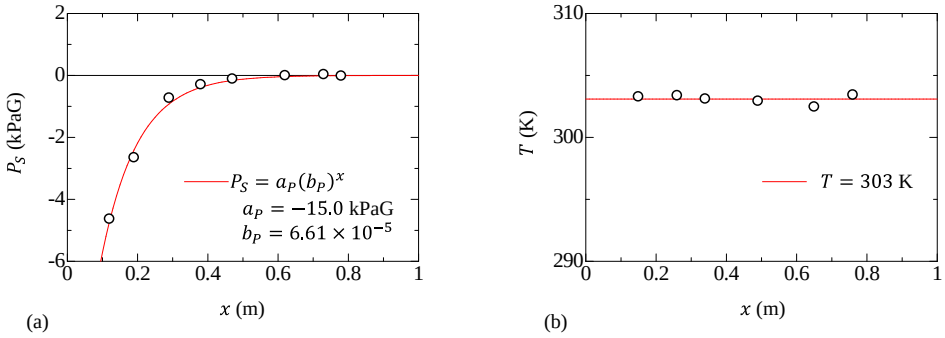

Fig. 9 Streamwise variations of (a) mean static pressure P_S and (b) mean temperature T.

3.2 Statistical stationarity

The plenum pressure remains approximately constant for a few seconds, suggesting that the flow in the test section is statistically steady for this period. This observation is corroborated by PIV data. Velocity vectors are measured at a sampling rate of 15 Hz. For each wind tunnel operation with a span of about 2 s, collected PIV images are divided into two equal sets, each comprising images captured during the early and late phases of the measurement period. The velocity statistics should be consistent across both datasets if the flow is statistically steady. The statistics are calculated using combined ensemble and spatial averages to minimize errors due to statistical convergence, as described by the following equation:

$$\overline{f} = \frac{1}{L_x L_y} \int_{y_1}^{y_2} \int_{x_1}^{x_2} \frac{1}{N_S} \sum_{n=1}^{N_S} f^{(n)}(x,y) dx dy, \tag{10}$$

where x_1, x_2, y_1, and y_2 specify the coordinates that define the measurement area, and $L_x = x_2 - x_1$ and $L_y = y_2 - y_1$ denote the dimensions of this area. For the PIV measurement location of $x_C = 0.465$ m, the average and rms fluctuations of streamwise velocity are $\overline{u} = 38.5$ m/s and $\sqrt{\overline{u^2} - \overline{u}^2} = 13.1$ m/s for the first dataset and $\overline{u} = 38.1$ m/s and $\sqrt{\overline{u^2} - \overline{u}^2} = 13.3$ m/s for the second dataset. These differences are minor and within the margin of error from the statistical uncertainty discussed

below. Similar results are also obtained at other measurement locations. Therefore, it is concluded that the flow is in a statistically steady state during the PIV measurement period.

3.3 Pressure and temperature profiles

Figure 9(a) presents the streamwise variation of the mean static pressure (gauge pressure), P_S. The pressure increases in the downstream direction and approaches the atmospheric pressure. The pressure distribution is well approximated by an exponential curve $P_S = a_P(b_P)^x$, where $a_P = -15.0$ kPaG and $b_P = 6.61 \times 10^{-5}$ are obtained with a least squares method. As the results are shown as gauge pressure, this pressure variation is slight compared to the atmospheric pressure and hardly affects the mean fluid density in the test section. Figure 9(b) presents the mean temperature T along the centerline. The streamwise variation of T is slight, and the average of all data points yields 303 K.

These measurement results enable us to estimate fluid density ρ with the equation of state for an ideal gas as $\rho = P/RT$ with the gas constant $R = 287.05$ J/kg K. Here, the exponential function $P_S = a_P(b_P)^x$ and mean temperature of 303 K are used to evaluate $\rho(x)$. The mean temperature yields the viscosity coefficient μ, calculated with Sutherland's law as

$$\mu = \mu_0 \left(\frac{T}{T_0} \right) \left(\frac{T_0 + S}{T + S} \right), \tag{11}$$

with $T_0 = 273$ K, $S = 110.4$ K, and $\mu_0 = 1.724 \times 10^{-5}$ Pa s. As the mean temperature does not vary with x, μ is also treated as a constant. These fluid properties are used in the analysis of velocity statistics obtained with the PIV.

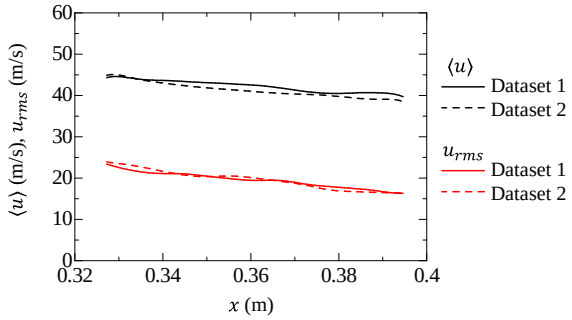

Fig. 10 Statistical convergence tests for mean velocity and rms velocity fluctuations with the PIV data measured at $(x_C, y_C) = (0.360\ \text{m},\ 0\ \text{m})$. Totally 700 vector snapshots are divided into two datasets, each containing 350 snapshots. The mean velocity and rms velocity fluctuations calculated separately for the two datasets are plotted as functions of x at $y = 0$.

3.4 Velocity statistics

The degree of statistical convergence is examined before the velocity statistics are discussed. For the measurement location of $(x_C, y_C) = (0.360\ \text{m},\ 0\ \text{m})$, 700 snapshots of velocity vectors are acquired. These snapshots are divided into two datasets, each containing 350 snapshots. The velocity statistics are separately calculated for the two datasets whose differences arise from statistical errors. Figure 10 compares the streamwise distributions of the average and rms fluctuations of streamwise velocity, $\langle u \rangle$ and u_{rms}, at $y = 0$. The two datasets yield slightly different distributions. A statistical quantity f calculated with datasets 1 and 2 is denoted by f_1 and f_2, respectively. For the distribution of f along the x axis at $y = 0$, the statistical error arising from the finite number of samples is evaluated with $f_1(x, 0)$ and $f_2(x, 0)$ as an rms error:

$$E(f) = \sqrt{\frac{1}{x_2 - x_1} \int_{x_1}^{x_2} (f_1 - f_2)^2 dx}, \tag{12}$$

where $x_1 \leq x \leq x_2$ is the measurement area. For Fig. 10, the relative errors, $E(\langle u \rangle)/\langle u \rangle$ and $E(u_{rms})/u_{rms}$, are about 5%, which is a typical statistical error when the number of the snapshots is about 350. Thus, statistical errors for the present PIV measurement with $N_S > 500$ are expected to be smaller than 5%. The statistical errors of other

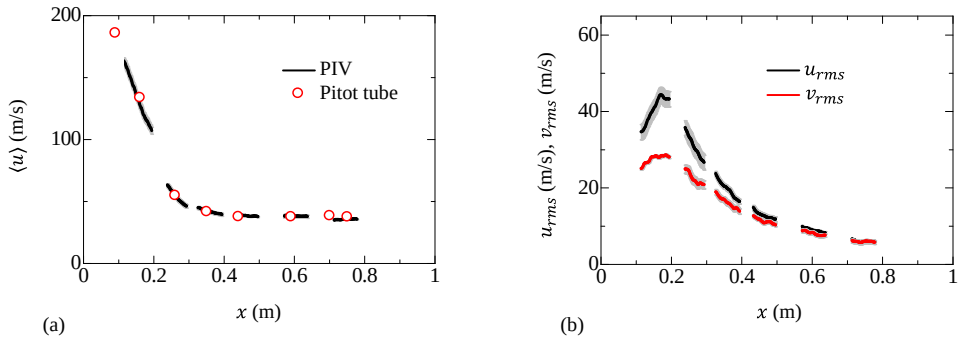

Fig. 11 Streamwise distributions of (a) mean streamwise velocity $\langle u \rangle$ and (b) rms velocity fluctuations of streamwise and vertical velocities, u_{rms} and v_{rms}, at $y = 0$. The gray shaded area represents the statistical errors estimated by Eq. (12).

velocity statistics are evaluated with this method for each PIV measurement location, and $E(f)$ is shown in figures below.

Figure 11(a) shows the streamwise distribution of mean streamwise velocity $\langle u \rangle$. The statistical errors estimated with Eq. (12) are shown in gray for PIV data. The mean velocity obtained with the Pitot tube is also plotted for comparison. For the Pitot tube measurement at $x = 0.09$ m, the PIV data for turbulence correction, Eq. (3), is unavailable. Therefore, an extrapolation of the PIV data provides the velocity variance used for the correction. The mean velocity distribution hardly differs for the PIV and the Pitot tube, ensuring the measurement accuracy of both methods. The mean velocity rapidly decreases in the x direction up to $x \approx 0.3$ m and then stays at an almost constant value of 37 m/s. For the region with the mean velocity exceeding 100 m/s ($x < 0.2$ m), conducting accurate PIV measurements is challenging because of the large Stokes number of tracer particles. However, it is worth mentioning that the droplets generated through condensation due to fluid expansion of supersonic flows are significantly smaller in diameter compared to the typical oil mists produced by fog generators, as discussed in Secs. 2.2. The mean velocity and velocity variances measured by the PIV agree with the pressure difference ΔP in Eq. (2) measured by the Pitot tube. These statistics are dominated by large-scale turbulent motion. The

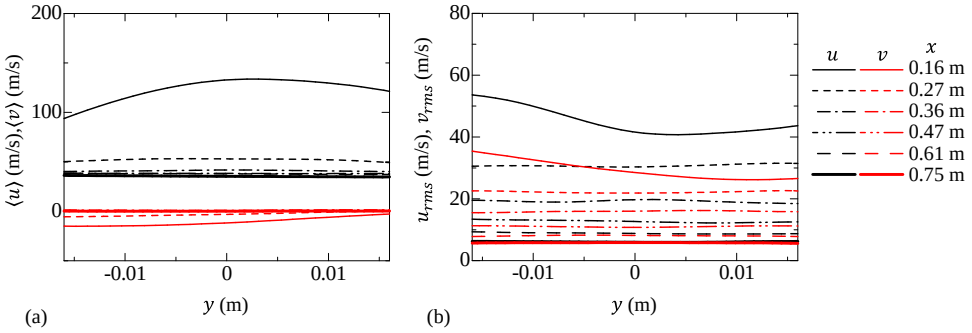

Fig. 12 Vertical distributions of (a) mean velocity and (b) rms velocity fluctuations for streamwise and vertical velocities.

comparison between the PIV and Pitot tube measurements indicates that the velocity statistics dominated by large scales are accurately evaluated with the PIV.

Figure 11(b) shows the distribution of rms velocity fluctuations of streamwise and vertical velocities, u_{rms} and v_{rms}. The rms velocity fluctuations increase with x for $x \lesssim 0.2$ m, where turbulence is generated. They continuously decay in the x direction after the peaks at $x \approx 0.2$ m. Although u_{rms} is much larger than v_{rms} in the upstream region, the difference between u_{rms} and v_{rms} becomes small with x. Their ratio u_{rms}/v_{rms} is often used to evaluate the isotropy at large scales. The average of u_{rms}/v_{rms} for $x > 0.4$ m is 1.08. This value is close to those in grid turbulence, for which $u_{rms}/v_{rms} \approx 1.1$ has been reported (Krogstad and Davidson, 2012; Isaza et al, 2014; Kitamura et al, 2014). Decaying turbulence generated by subsonic jet interaction was investigated in Tan et al (2023). They also reported that u_{rms} is larger than v_{rms} with $u_{rms}/v_{rms} \approx 1.16$. Thus, grid turbulence and turbulence generated by jet interaction have a similar degree of isotropy.

Figure 12 shows the vertical distributions of mean velocities, $\langle u \rangle$ and $\langle v \rangle$, and rms velocity fluctuations, u_{rms} and v_{rms}. At $x = 0.16$ m, the mean velocity varies significantly with y. The y dependence of the mean velocity becomes weak as x increases. For $x \geq 0.36$ m, $\langle u \rangle$ and $\langle v \rangle$ are almost uniform in both x and y directions, and the

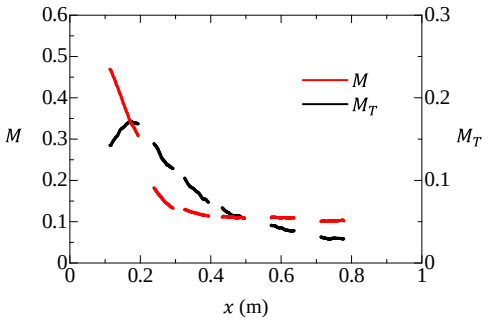

Fig. 13 Streamwise variations of the mean flow Mach number M and turbulent Mach number M_T at $y = 0$.

mean velocity gradient is negligible in the downstream region. The rms velocity fluctuations are also inhomogeneous in the y direction at $x = 0.16$ m, where u_{rms} and v_{rms} are large away from the center ($y = 0$). Large u_{rms} and v_{rms} at $x = 0.16$ m appear in the region of y with the large mean velocity gradient $\partial\langle u\rangle/\partial y$, and the production of turbulent kinetic energy due to the mean shear still influences the flow at $x = 0.16$ m. The rms velocity fluctuations become homogeneous in the y direction for $x \geq 0.27$ m. These results suggest the nearly homogeneous and isotropic turbulence with a uniform mean flow forms for $x \gtrsim 0.35$ m.

Figure 13 presents the spatial variations of the mean flow Mach number $M = \langle u\rangle/a$ and the turbulent Mach number $M_T = \sqrt{u_{rms}^2 + 2v_{rms}^2}/a$ defined using the speed of sound a corresponding to mean temperature T, where $u_{rms}^2 + 2v_{rms}^2$ is twice the turbulent kinetic energy. For the present measurement region, M_T reaches its peak of about 0.17 and subsequently decreases with x as the turbulence decays. The turbulent Mach number characterizes the local effects of compressibility. Local turbulent motions in regions of high M_T lead to fluid expansion and compression, thereby inducing density fluctuations. For example, shocklets emerge in statistically steady HIT driven by solenoidal forcing when $M_T \gtrsim 0.6$ (Watanabe et al, 2021). Such local compressibility effects are negligible in the decay region because of low M_T. This is similar in compressible grid turbulence in other studies (Zwart et al, 1997; Briassulis et al, 2001).

The maximum mean flow Mach number reported in Zwart et al (1997) is $M = 0.7$. However, the local compressibility effects on freely decaying turbulence are related to M_T rather than M. Typically, fully-developed grid turbulence exhibits a turbulence intensity $u_{rms}/\langle u \rangle$ less than 0.05 (Melina et al, 2016; Nagata et al, 2017), indicating that grid turbulence with $M = 0.7$ has $M_T < 0.06$, similar to that in the present experiments. In facilities designed for studying decaying turbulence, attaining a high turbulent Mach number may be impractical due to the inherently low turbulence intensity. Nonetheless, Zwart et al (1997) observed that the decay of compressible grid turbulence at low M_T differs from incompressible cases. These compressibility effects at low M_T are likely associated with the turbulence generation process near the grid. When comparing grid turbulence with jet interaction in terms of turbulence generation, the Mach number defined using the mean velocity between grid bars is important. In subsonic cases, the flow accelerates when passing between grid bars, with the mean velocity between the bars reaching about 1.4 times that in the decay region (Melina et al, 2016). This factor depends on grid geometry but is typical for conventional square grids that produce isotropic turbulence (solidity of about 0.3). For $M = 0.7$, the Mach number associated with the mean shear near the grid is approximately estimated as $M_S \approx 1.4M = 0.98$, which is related to the convective Mach number used to assess the compressibility effects on shear flows (Papamoschou and Roshko, 1988). M_S corresponds to the jet Mach number $M_J = 1.36$ in the supersonic jet interaction. The compressibility effects on turbulence generation are characterized by M_S and M_J because of the production of turbulent kinetic energy arising from the mean shear near the grid or jet nozzles. Therefore, in terms of M_S and M_T, the compressibility effects in the present experiments are comparable, if not more significant, than those observed in Zwart et al (1997). Grid turbulence generated in shock tubes is expected to be less influenced by compressibility because of the lower mean flow Mach number, resulting in lower M_S and M_T (Briassulis et al, 2001; Fukushima et al, 2021).

In facilities examining decaying turbulence, the nonlocal compressibility effects on the decay stemming from the turbulence generation process can be categorized into two types. The first is the direct impact on the generated turbulence, which leads to variances in large-scale dynamics. In incompressible flows, the decay characteristics of HIT differ between Saffman and Batchelor turbulence, owing to their distinct three-dimensional energy spectra at low wavenumbers (Davidson, 2004). This disparity originates from the differing injection of linear and angular momentum during the turbulence generation process. The second type of influence is wave propagation. Most wind tunnel facilities designed for decaying turbulence induce turbulence through the introduction of mean shear at the entrance of the test section. In the multiple-supersonic-jet wind tunnel, the mean shear of each supersonic jet initially generates turbulence. Each jet can produce shock waves when the Mach number is sufficiently high. Similar pressure waves are also anticipated in compressible grid turbulence, especially since the Mach number related to the mean shear near the grid can be high. The pressure waves induced by the supersonic jets resemble spherical shock waves and consist of a pronounced compression with a quasi-discontinuous pressure rise, followed by a blunt expansion (Williams et al, 1975; Nichols et al, 2013). Therefore, while the shock wave propagation may not significantly alter the mean density and pressure, it can influence the small-scale properties of turbulence (Watanabe et al, 2021). The decay law of HIT is sensitive to the scaling of the turbulent kinetic energy dissipation rate (Krogstad and Davidson, 2010). The pressure waves generated near the nozzles can propagate through the decay region with low M_T, possibly leading to turbulence decay behavior that diverges from incompressible cases.

Figure 14 shows the streamwise distribution of skewness S and flatness F of velocity components. A variable with a probability distribution following a Gaussian function has $S = 0$ and $F = 3$, shown as horizontal lines in Fig. 14. These Gaussian values

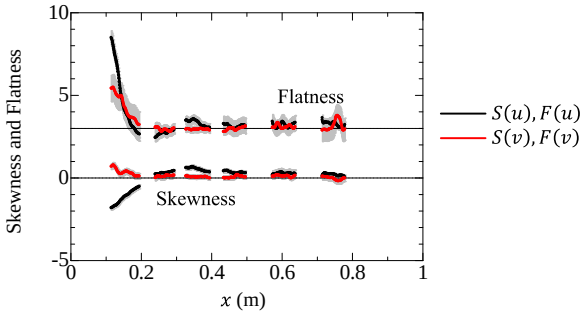

Fig. 14 Streamwise distributions of skewness and flatness of streamwise and vertical velocities at $y = 0$.

of S and F have been obtained for various types of fully-developed isotropic turbulence (Hwang and Eaton, 2004; Krogstad and Davidson, 2010). For the present facility, S and F greatly differ from the Gaussian values in the upstream region of $x \lesssim 0.15$ m. The flow is highly inhomogeneous and anisotropic in this region. Large F is related to the intermittency of large-scale fluctuations. The intermittent behavior of the jet interaction may cause large values of $F(u)$ and $F(v)$, as also reported for the interaction of two incompressible jets (Zhou et al, 2018). As turbulence develops, S and F approach the Gaussian values, and $S \approx 0$ and $F \approx 3$ are achieved for $x \gtrsim 0.2$ m. Therefore, the intermittent velocity fluctuations become insignificant in the decay region.

The large-scale turbulent motion is characterized by integral scales, which can be evaluated with velocity auto-correlation functions. The longitudinal auto-correlation functions for streamwise and vertical velocities are respectively defined as

$$f_u(x, y, r_x) = \frac{\langle u'(x, y)u'(x + r_x, y)\rangle}{\langle u'^2(x, y)\rangle}, \tag{13}$$

$$f_v(x, y, r_y) = \frac{\langle v'(x, y)v'(x, y + r_y)\rangle}{\langle v'^2(x, y)\rangle}, \tag{14}$$

where r_x and r_y are separation distances. Because the PIV measures the velocity profiles in a finite area, the available ranges of r_x and r_y are limited. For evaluations of

the correlation function with large distances, $f_u(r_x)$ is calculated for (x, y) corresponding to a location near the upstream end of the measurement area at $y = 0$. Similarly, $f_v(r_y)$ is calculated for (x, y) corresponding to the upstream bottom corner of the measurement area. In this way, r_x and r_y range up to the size of the measurement area.

The longitudinal integral scales are defined as the integrals of f_u and f_v:

$$L_u = \int_0^{r_{x0}} f_u dr_x, \quad L_v = \int_0^{r_{y0}} f_v dr_y. \tag{15}$$

Here, r_{x0} and r_{y0} are often taken as the first zero-crossing point (Briassulis et al, 2001). For the present PIV, the measurement area is insufficient to calculate the correlation functions up to the zero-crossing point. In addition, as also observed for hot-wire measurements in wind tunnels, an accurate evaluation of correlation functions for large r_x and r_y is problematic because of a limited number of large-scale samples. For these reasons, the integral scale is often evaluated by approximating the correlation function at large r with an exponential function (Morikawa et al, 2008; Bewley et al, 2012; Griffin et al, 2019). The present study also adapts this methodology for the calculation of integral scales. An exponential function $a_f \exp(-b_f r_x)$ is obtained with a least squares method applied for measured f_u in the range of r_x with $f_u < 0.5$. The numerical integration of f_u is calculated with the measured f_u and the exponential function as

$$L_u = \int_0^{r_{1/2}} f_u dr_x + \int_{r_{1/2}}^{r_{end}} a_f \mathrm{e}^{-b_f r_x} dr_x, \tag{16}$$

where $r_{1/2}$ is defined as $f_u(r_{1/2}) = 0.5$ and r_{end} corresponds to r_x where $a_f \exp(-b_f r_x)$ is equal to 10^{-5}. Because of the exponential decay of the correlation, larger values of r_{end} do not affect the evaluation of the integral scale. The integral scale in the vertical direction L_v is also calculated by the same method applied for f_v.

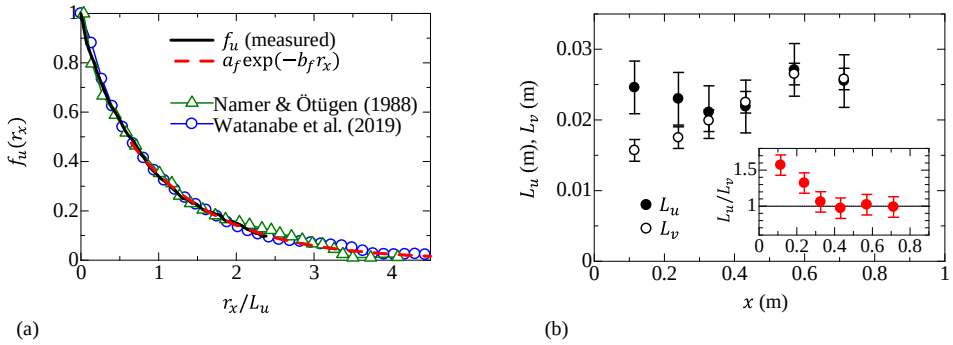

Fig. 15 (a) Longitudinal auto-correlation function of streamwise velocity at $x = 570$ mm and $y = 0$ mm. The measured correlation is compared with an exponential function $f_u = a_f \exp(-b_f r_x)$ and the correlation functions in incompressible turbulent jets (Namer and Ötügen 1988; Watanabe et al 2019). A least squares method determines $a_f = 0.843$ and $b_f = -32.8$ m^{-1} from the measured f_u. The separation distance r_x is normalized by the integral scale L_u. (b) The streamwise variation of integral scales L_u and L_v, which are calculated from the longitudinal auto-correlation functions of streamwise and vertical velocities, respectively. The inset shows the ratio between L_u and L_v.

Figure 15(a) shows the correlation function f_u and its approximation based on the exponential function at $(x, y) = (570\ \text{mm}, 0\ \text{mm})$. The separation distance r_x is normalized with the integral scale for comparisons with other turbulent flows. The exponential function accurately approximates the decay of f_u for large r_x. In addition, the profile of f_u agrees well with the correlation functions measured in other turbulent flows.

Figure 15(b) presents the streamwise variation of the integral scales. In the inhomogeneous and anisotropic region, $x < 0.3$ m, the streamwise integral scale L_u is larger than the vertical scale L_v, and large-scale velocity fluctuations are also anisotropic. On the other hand, the downstream region satisfies $L_u \approx L_v$. This is also confirmed by the inset presenting L_u/L_v. The average of L_u/L_v for $x > 0.3$ m is 1.03, and the integral scales hardly differ in both directions, suggesting that turbulent motion at large scales is statistically isotropic. For $0.3\ \text{m} \lesssim x \lesssim 0.6$ m, the integral scales increase as turbulence decays. However, in the most downstream location of the measurement, L_u and L_v decrease with x. In DNS of decaying isotropic turbulence in a triply periodic domain, the decay is influenced by the boundary conditions when the domain

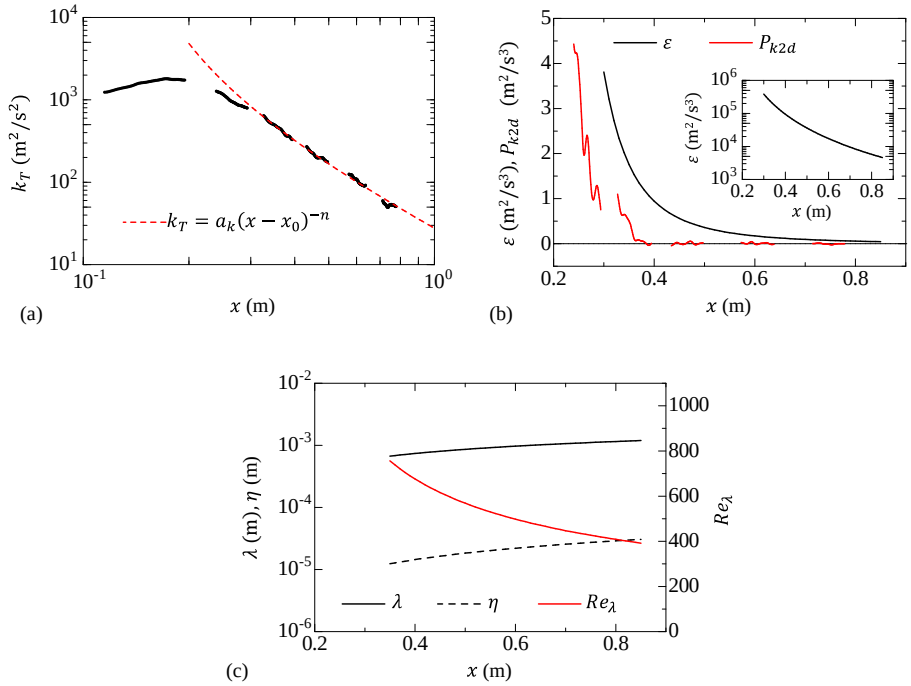

Fig. 16 (a) The decay of turbulent kinetic energy k_T along the centerline. The red broken line represents a power law $k_T = a_k(x - x_0)^{-n}$ with $a_k = 21.0$ m^2/s^2, $x_0 = 0.12$ m, and $n = 2.1$, which are obtained with a least squares method applied for $x > 0.32$ m. (b) The streamwise variations of the turbulent kinetic energy dissipation rate ε, estimated with the power law decay of k_T, and the two-dimensional component of the production term of k_T, P_{k2d}. (c) Taylor microscale λ, Kolmogorov scale η, and turbulent Reynolds number Re_λ for $x \geq 0.35$ m.

size divided by the integral scale is smaller than about 3 (Anas et al, 2020). The side length of the cross-section, 0.1 m, is about $3.7L_u$ at $x = 0.57$ m. The decrease of L_u and L_v in the further downstream region may be caused by the confinement effects.

3.5 The dissipation rate of turbulent kinetic energy

Figure 16(a) shows the streamwise variation of turbulent kinetic energy per unit mass $k_T \approx (\langle u'^2 \rangle + 2\langle v'^2 \rangle)/2$ along the centerline. The decay of k_T is investigated for $x > 0.32$ m. A nonlinear least squares method (Levenberg–Marquardt method) applied for $x > 0.32$ m yields the parameters in the power law, Eq. (7), as $a_k = 21.0$ m^2/s^2, $x_0 = 0.12$ m, and $n = 2.1$. Equation (7) with these parameters is also shown in the figure. The decay of k_T is well approximated by the power law. The exponent

$n = 2.1$ is larger than typical values reported for incompressible grid turbulence at high Reynolds numbers, $n \approx 1.0$–1.5 (Kistler and Vrebalovich, 1966; Kang et al, 2003; Thormann and Meneveau, 2014; Zheng et al, 2021b). As discussed in Sect. 1, Zwart et al (1997) also reported that n in compressible grid turbulence tends to be larger than incompressible cases. This tendency is qualitatively consistent with the large exponent in this study. However, these results contradict the decrease of n observed in shock-tube experiments (Briassulis et al, 2001; Fukushima et al, 2021), and the compressibility effects on the decay exponent should be addressed in future studies. Tan et al (2023) observed that the decay exponent in incompressible decaying turbulence, generated by jet grids that emit round jets from grid bars, is approximately 2, which is also larger than conventional grid turbulence. This finding indicates that the interaction of jets may also play a significant role in influencing the decay exponent.

Figure 16(b) shows the streamwies variation of the dissipation rate ε estimated from the decay of k_T with Eq. (8). One of the assumptions for the dissipation estimation is the homogeneity of mean velocity to assure that the production of k_T is negligible. However, the mean streamwise velocity decays with x in the upstream region. To validate the assumption, the two-dimensional component of the production term in Eq. (5) is evaluated as

$$P_{k2d} = -\langle u'^2 \rangle \frac{\partial \langle u \rangle}{\partial x} - \langle u'v' \rangle \frac{\partial \langle u \rangle}{\partial y} - \langle v'u' \rangle \frac{\partial \langle v \rangle}{\partial x} - \langle v'^2 \rangle \frac{\partial \langle v \rangle}{\partial y}, \tag{17}$$

where the velocity gradients are calculated with a conventional fourth-order central difference. Figure 16(b) compares the streamwise variation of P_{k2d} at $y = 0$ with ε. The oscillation of P_{k2d} is due to the finite difference approximation for the mean velocity gradient with a limited number of samples. However, the results are still useful to examine the validity of the estimation of ε. We have confirmed that the first term in Eq. (17) has a dominant contribution to P_{k2d}. Positive P_{k2d} is attributed to the decay

of $\langle u \rangle$ observed in Fig. 11(a). As $\langle u \rangle$ approaches a constant value with x increasing, P_{k2d} rapidly decays with x. For $x \gtrsim 0.35$ m, P_{k2d} is negligibly small compared to the dissipation rate, estimated with the mean flow advection of k_T. This comparison of P_{k2d} and ε and other statistics discussed above suggest that nearly homogeneous and isotropic turbulence has developed at around $x = 0.35$ m with only a slight violation of statistical homogeneity and isotropy.

The production of turbulent kinetic energy becomes negligible at a streamwise distance of $x \gtrsim 0.35$ m. Considering the nozzle spacing of $D_J = 0.012$ m, this distance corresponds to $x/D_J = 29.2$. Tan et al (2023) have demonstrated that, in turbulence generated by jet grids, the streamwise location where the flow attains statistical homogeneity is dependent on the jet spacing. They found that homogeneity is achieved at a distance considerably shorter than $x/D_J = 29.2$. It is well documented that the turbulent transition of a supersonic jet tends to be delayed as the jet Mach number increases (Bogdanoff, 1983; Nagata et al, 2018). The extensive distance required for achieving statistical homogeneity in the supersonic jet interaction is attributed to the slow development of the supersonic jets. Consistently, an increase in the virtual origin of turbulent kinetic energy decay has been reported in compressible grid turbulence as the mean flow Mach number increases (Briassulis et al, 2001).

The small-scale turbulence properties are often related to the kinetic energy dissipation rate. The Taylor microscale λ and Kolmogorov scale η are defined as

$$\lambda = \sqrt{\frac{10\mu k_T}{\rho\varepsilon}}, \tag{18}$$

$$\eta = (\mu/\rho)^{3/4}\varepsilon^{-1/4}. \tag{19}$$

The turbulent Reynolds number Re_λ is define with λ as

$$Re_\lambda = \frac{\rho\sqrt{2k_T/3}\lambda}{\mu}. \tag{20}$$

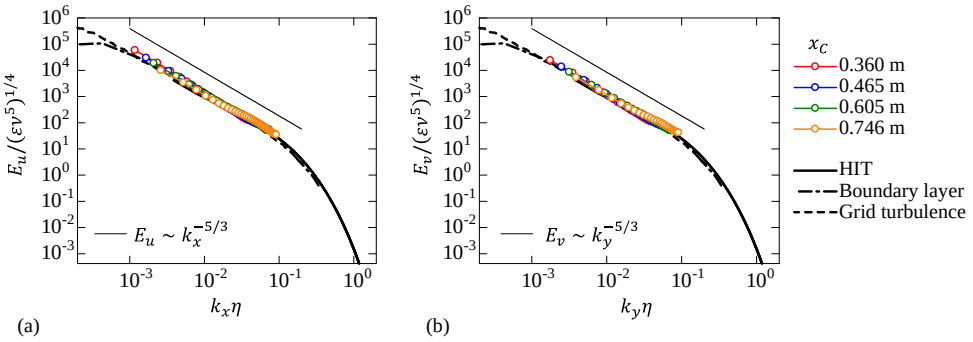

Fig. 17 Normalized energy spectra of (a) streamwise velocity, $E_u(k_x)$, and (b) vertical velocity, $E_v(k_y)$, where k_x and k_y are the wavenumbers in the streamwise and vertical directions, respectively. The spectra and wavenumbers are non-dimensionalized with the kinematic viscosity $\nu = \mu/\rho$, the energy dissipation rate per unit mass ε, and the Kolmogorov scale η. The present results are compared with direct numerical simulation of forced HIT ($Re_\lambda = 202$) (Watanabe and Nagata, 2023) and experiments of a boundary layer ($Re_\lambda = 202$) (Saddoughi and Veeravalli, 1994; Nieuwstadt and Boersma, 2016) and grid turbulence ($Re_\lambda = 520$) (Kistler and Vrebalovich, 1966).

The dissipation rate estimated from the decay of k_T with Eq. (8) is used to evaluate λ, η, and Re_λ in the nearly homogeneous and isotropic region of $x \geq 0.35$ m. Figure 16(c) shows their streamwise variations of λ, η, and Re_λ. The length scales, λ, and η, increase as turbulence decays in the x direction. The orders of λ and η are $O(10^{-3}$ m) and $O(10^{-5}$ m), respectively. The spatial resolution of PIV is about 1.0×10^{-3} m, and the scales greater than the Taylor microscale are resolved by the PIV. This resolution is sufficient to investigate the large-scale properties, such as mean velocity and rms velocity fluctuations. The turbulent Reynolds number decreases with the decay of turbulence. It ranges between about 750 and 400 for $x \geq 0.35$ m. These values of Re_λ are larger than those of most subsonic grid turbulence in large wind tunnel facilities because of the large velocity fluctuations of supersonic jets.

One-dimensional energy spectra of streamwise and vertical velocities (E_u and E_v) are calculated with Fourier transform in the x and y directions, respectively. The wavenumbers in these directions are denoted by k_x and k_y. The energy spectra in turbulence with a high Reynolds number are known to have a universal shape in an inertial subrange in various turbulent flows (Pope, 2000). Figure 17 presents E_u and

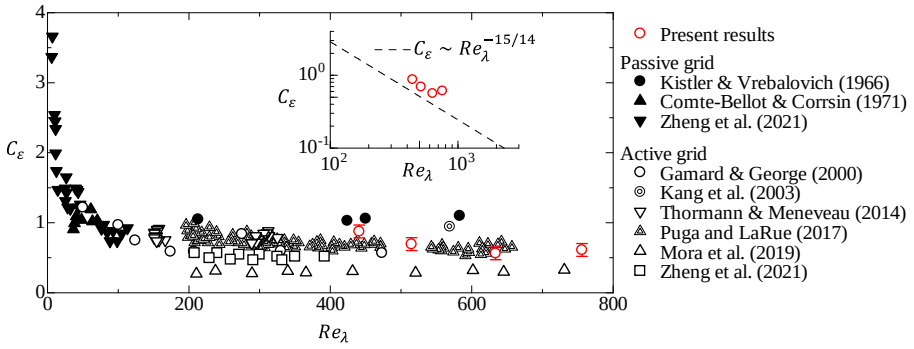

Fig. 18 Dependence of non-dimensional energy dissipation rate C_ε on the turbulent Reynolds number Re_λ. The present results are compared with experimental data of subsonic grid turbulence: Kistler and Vrebalovich (1966), Comte-Bellot and Corrsin (1971), and Zheng et al (2021a) for passive-grid generated turbulence; Gamard and George (2000), Kang et al (2003), Thormann and Meneveau (2014), Puga and LaRue (2017), Mora et al (2019), and Zheng et al (2021b) for active-grid generated turbulence. The inset shows the Re_λ dependence of C_ε in logarithmic scales. The broken line indicates the scaling for non-equilibrum turbulence, $C_\varepsilon \sim Re_\lambda^{-15/14}$ (Bos and Rubinstein, 2017).

E_v measured at several streamwise locations. The spectra and wavenumbers are normalized by the dissipation rate ε and kinematic viscosity $\nu = \mu/\rho$. The present results are compared with incompressible turbulent flows. The spectra are evaluated for normalized wavenumbers between 10^{-3} and 10^{-1}, determined by the measurement area and spatial resolution. The present results quantitatively agree with other turbulent flows. The consistency of these normalized spectra serves as additional validation for the dissipation estimation. They are also consistent with the power laws expected for the inertial subrange, $E_u \sim k_x^{-5/3}$ and $E_v \sim k_y^{-5/3}$. Thus, the present PIV with condensation particles is capable of measuring the scale dependence of velocity fluctuations in the inertial subrange. In addition, the flow at a wide range of scales is in a statistically isotropic state, as attested by $E_u \approx E_v$.

The dissipation rate is often related to characteristic velocity $\mathcal{U}$ and lenght $\mathcal{L}$ of large-scale turbulent motion as

$$\varepsilon = C_\varepsilon \frac{\mathcal{U}^3}{\mathcal{L}}, \tag{21}$$

where C_ε is a non-dimensional dissipation rate. C_ε plays a central role in theories and models of turbulent flows (Vassilicos, 2015). The velocity and length scales in the present experiment are evaluated as $\mathcal{U} = \sqrt{(\langle u'^2 \rangle + \langle v'^2 \rangle)/2}$ and $\mathcal{L} = (L_u + L_v)/2$, and C_ε is evaluated with ε in the nearly homogeneous and isotropic region. Figure 18 plots C_ε as a function of Re_λ for the present experiment and other studies of incompressible grid turbulence. Here, C_ε is evaluated at $x = 0.35$ m, 0.43 m, 0.57 m, and 0.72 m. For $x = 0.35$ m, the integral scale is evaluated with a linear approximation for the values at $x = 0.33$ m and 0.43 m in Fig. 15(b). In fully-developed grid turbulence with high Re_λ in incompressible flows, C_ε takes values approximately between 0.4 and 1.1 while C_ε increases rapidly as Re_λ becomes smaller than about 100. The present values of $C_\varepsilon = 0.56$–0.87 are within a range reported for grid turbulence with high Re_λ. The decay exponent of the turbulent kinetic energy is known to be influenced by the spatial variation of C_ε. For the present experiment, C_ε slightly increases in the streamwise direction. The increase of C_ε causes a larger decay exponent n (Krogstad and Davidson, 2010). The spatial variation of C_ε is possibly relevant to the large values of n in the present experiment and in compressible grid turbulence (Zwart et al, 1997).

The observed increase of C_ε with x may be associated with non-equilibrium turbulence. Studies on grid turbulence and unsteady turbulence in incompressible fluids have identified a non-equilibrium regime of energy cascade characterized by $C_\varepsilon \sim Re_\lambda^{-1}$ (Valente and Vassilicos, 2014; Valente et al, 2014; Vassilicos, 2015). Consistently, a similar scaling of $C_\varepsilon \sim Re_\lambda^{-15/14}$ was theoretically proposed in Bos and Rubinstein (2017). As Re_λ decreases with the decay of turbulence, this non-equilibrium scaling could be relevant to the observed increase in the decay exponent. The inset of Fig. 18 depicts $C_\varepsilon(Re_\lambda)$ in logarithmic scales. The present data align with the non-equilibrium scaling $C_\varepsilon \sim Re_\lambda^{-15/14}$. Zwart et al (1997) noted an increase in the decay exponent n at sufficiently high mean flow Mach numbers. As discussed earlier, the turbulent Mach number in their experiments was low enough for local compressibility

effects to be negligible, suggesting that the increased n resulted from compressibility effects during the turbulence generation process. In the case of incompressible grid turbulence, the non-equilibrium region is typically found near the grid. Furthermore, experiments with various grids have established that the extent of the non-equilibrium region is dependent on grid geometry (Valente and Vassilicos, 2014). The findings from our experiments, along with those in Zwart et al (1997) with varied Mach numbers, imply that compressibility effects in the turbulence generation process may lead to a spatial extension of the non-equilibrium region.

4 Conclusion

The present study has reported the development and characterization of the multiple-supersonic-jet wind tunnel, where the interaction of 36 supersonic jets generates turbulence that decays in the streamwise direction. The PIV, pitot tube, and thermocouple measurements characterize the generated turbulence, where velocity vectors, static and dynamic pressures, and temperature are measured. The present wind tunnel can sustain a steady mean flow over 2–3 s. It can also seed tracer particles in the test section by condensation. The accuracy of the PIV is confirmed by comparing the velocity statistics with other turbulent flows. In addition, the mean velocity measured by the PIV agrees well with the Pitot tube measurements for which turbulence correction is applied with the PIV data of velocity variances.

The mean velocity in the upstream region is large along the centerline of the test section. However, as the flow evolves, the mean velocity profile becomes uniform in the test section. Then, the mean velocity gradient becomes small in the downstream region, where the production term of turbulent kinetic energy is negligible. At this decay regime, rms velocity fluctuations are also uniform in the cross-section. The ratio of rms values of streamwise- and vertical-velocity fluctuations is about 1.08, close to the values reported for incompressible grid turbulence. The longitudinal integral

length scales are also similar in the streamwise and vertical directions. These statistics have confirmed that the supersonic jet interaction generates nearly homogeneous and isotropic turbulence. In the inhomogeneous and anisotropic region near the jet nozzles, the flatness of velocity fluctuations is larger than 3, indicating that the large-scale velocity fluctuations are highly intermittent. The skewness and flatness of velocity fluctuations are close to the Gaussian values in the decay region, where the large-scale intermittency is insignificant.

The decay of turbulent kinetic energy per unit mass is investigated in the nearly homogeneous and isotropic region. The turbulent kinetic energy decays according to a power law, as reported for subsonic grid turbulence. The decay exponent n for the supersonic jet interaction is about 2, which is larger than the values reported for incompressible grid turbulence. This large value of n is consistent with experiments of compressible grid turbulence in a high-speed wind tunnel by Zwart et al (1997). In addition, the dissipation rate of turbulent kinetic energy per unit mass has been evaluated with the decay of the turbulent kinetic energy. The energy spectra of velocity fluctuations normalized by the dissipation rate and kinematic viscosity follow the universal power law of the inertial subrange observed for other incompressible turbulent flows. The non-dimensional dissipation rate C_ε for the supersonic jet interaction is within a range of 0.51–0.87, which is also consistent with grid turbulence at a high Reynolds number. The streamwise increase of C_ε aligns with the non-equilibrium scaling of $C_\varepsilon \sim Re_\lambda^{-15/14}$, which can lead to the large decay exponent.

These results have demonstrated that the multiple-supersonic-jet wind tunnel is helpful in the investigation of decaying homogeneous and isotropic turbulence whose generation process is strongly influenced by fluid compressibility. The nozzle component in the present wind tunnel can be replaced with other components with different nozzle geometries, generating turbulent jets with different Mach and Reynolds numbers. This feature is helpful in varying the degree of the compressibility effects, which will be considered in future studies.

Statements and Declarations

Funding

This work was supported by Japan Society for the Promotion of Science (KAKENHI Grant Numbers JP22K03903 and JP22H01398).

Competing interests

The authors have no competing interests to declare that are relevant to the content of this article.

Availability of data and materials

The data that support the findings of this study are available from the corresponding author upon reasonable request.

Authors' contributions

Takahiro Mori: Data curation (equal); Formal Analysis (equal); Investigation (lead); Methodology (equal); Resources (equal); Software (supporting); Validation (equal); Visualization (equal); Writing - original draft (supporting); Writing - review & editing (equal). **Tomoaki Watanabe**: Conceptualization (lead); Data curation (equal); Formal Analysis (equal); Funding acquisition (equal); Investigation (supporting); Methodology (equal); Project administration (lead); Resources (equal); Software (lead); Supervision (lead); Validation (equal); Visualization (equal); Writing - original draft (lead); Writing - review & editing (equal). **Koji Nagata**: Conceptualization (supporting); Data curation (supporting); Funding acquisition (equal); Investigation (supporting); Methodology (supporting); Project administration (supporting); Resources (equal); Software (supporting); Supervision (supporting); Validation (equal); Visualization (supporting); Writing - original draft (supporting); Writing - review & editing (equal).

Acknowledgments. The authors acknowledge Prof. K. Mori (Osaka Prefecture University), Mr. N. Iwakura (Nagoya University), and Ms. R. Nakayama (Nagoya University) for their help and valuable comments in developing the multiple-supersonic-jet wind tunnel. The authors also acknowledge Mr. K. Ishizawa (Nagoya University) for assistance in experiments.

References

Agui JH, Briassulis G, Andreopoulos Y (2005) Studies of interactions of a propagating shock wave with decaying grid turbulence: velocity and vorticity fields. J Fluid Mech 524:143–195

Anas M, Joshi P, Verma MK (2020) Freely decaying turbulence in a finite domain at finite Reynolds number. Phys Fluids 32(9):095109

Anderson JD (1990) Modern compressible flow: with historical perspective, vol 12. McGraw-Hill New York

Bailey SCC, Hultmark M, Monty JP, et al (2013) Obtaining accurate mean velocity measurements in high reynolds number turbulent boundary layers using Pitot tubes. J Fluid Mech 715:642–670

Batchelor GK (1953) The theory of homogeneous turbulence. Cambridge university press

Bellani G, Variano EA (2014) Homogeneity and isotropy in a laboratory turbulent flow. Exp Fluids 55(1):1–12

Bewley GP, Chang K, Bodenschatz E (2012) On integral length scales in anisotropic turbulence. Phys Fluids 24(6)

Bogdanoff DW (1983) Compressibility effects in turbulent shear layers. AIAA J 21(6):926–927

Bos WJT, Rubinstein R (2017) Dissipation in unsteady turbulence. Phys Rev Fluids 2(2):022601

Bos WJT, Chevillard L, Scott JF, et al (2012) Reynolds number effect on the velocity increment skewness in isotropic turbulence. Phys Fluids 24(1)

Bradshaw P (1977) Compressible turbulent shear layers. Annu Rev Fluid Mech 9(1):33–52

Briassulis G, Agui JH, Andreopoulos Y (2001) The structure of weakly compressible grid-generated turbulence. J Fluid Mech 432:219–283

Canuto VM (1997) Compressible turbulence. Astrophys J 482(2):827

Carter D, Petersen A, Amili O, et al (2016) Generating and controlling homogeneous air turbulence using random jet arrays. Exp Fluids 57(12):1–15

Clemens NT, Mungal MG (1991) A planar Mie scattering technique for visualizing supersonic mixing flows. Exp Fluids 11(2-3):175–185

Comte-Bellot G, Corrsin S (1966) The use of a contraction to improve the isotropy of grid-generated turbulence. J Fluid Mech 25(4):657–682

Comte-Bellot G, Corrsin S (1971) Simple Eulerian time correlation of full-and narrow-band velocity signals in grid-generated, 'isotropic' turbulence. J Fluid Mech 48(2):273–337

Crittenden TM, Glezer A (2006) A high-speed, compressible synthetic jet. Phys Fluids 18(1):017107

Davidson PA (2004) Turbulence: An Introduction for Scientists and Engineers. Oxford Univ. Pr.

Davidson PA (2009) The role of angular momentum conservation in homogeneous turbulence. J Fluid Mech 632:329–358

Djenidi L, Kamruzzaman M, Antonia RA (2015) Power-law exponent in the transition period of decay in grid turbulence. J Fluid Mech 779:544–555

Donzis DA, John JP (2020) Universality and scaling in homogeneous compressible turbulence. Phys Rev Fluids 5(8):084609

Foelsch K (1949) The analytical design of an axially symmetric laval nozzle for a parallel and uniform jet. J Aeronaut Sci 16(3):161–166

Fukushima G, Ogawa S, Wei J, et al (2021) Impacts of grid turbulence on the side projection of planar shock waves. Shock Waves 31(2):101–115

Gamard S, George WK (2000) Reynolds number dependence of energy spectra in the overlap region of isotropic turbulence. Flow, Turbul Combust 63:443–477

Griffin KP, Wei NJ, Bodenschatz E, et al (2019) Control of long-range correlations in turbulence. Exp Fluids 60:1–14

Gad-el Hak M, Corrsin S (1974) Measurements of the nearly isotropic turbulence behind a uniform jet grid. J Fluid Mech 62(1):115–143

Honkan A, Andreopoulos J (1992) Rapid compression of grid-generated turbulence by a moving shock wave. Phys Fluids 4(11):2562–2572

Hwang W, Eaton JK (2004) Creating homogeneous and isotropic turbulence without a mean flow. Exp Fluids 36(3):444–454

Isaza JC, Salazar R, Warhaft Z (2014) On grid-generated turbulence in the near-and far field regions. Journal of Fluid Mechanics 753:402–426

Ishida T, Hayashi Y, Saito T, et al (2023) Gas leakages from gastrointestinal endoscopy system–its visualization and semi-quantification utilizing schlieren optical system in the swine models. Surg Endosc 37(3):1718–1726

Kang HS, Chester S, Meneveau C (2003) Decaying turbulence in an active-grid-generated flow and comparisons with large-eddy simulation. J Fluid Mech 480:129–160

Kistler AL, Vrebalovich T (1966) Grid turbulence at large Reynolds numbers. J Fluid Mech 26(1):37–47

Kitamura T, Nagata K, Sakai Y, et al (2014) On invariants in grid turbulence at moderate Reynolds numbers. J Fluid Mech 738:378–406

Kouchi T, Fukuda S, Miyai S, et al (2019) Acetone-condensation nano-particle image velocimetry in a supersonic boundary layer. In: AIAA Scitech 2019 Forum, p 1821

Krogstad PÅ, Davidson PA (2010) Is grid turbulence Saffman turbulence? J Fluid Mech 642:373–394

Krogstad PÅ, Davidson PA (2012) Near-field investigation of turbulence produced by multi-scale grids. Phys Fluids 24(3):035103

Larssen JV, Devenport WJ (2011) On the generation of large-scale homogeneous turbulence. Exp Fluids 50:1207–1223

Lee S, Lele SK, Moin P (1991) Eddy shocklets in decaying compressible turbulence. Phys Fluids 3(4):657–664

Lohse D (1994) Crossover from high to low Reynolds number turbulence. Phys Rev Lett 73(24):3223

Makita H (1991) Realization of a large-scale turbulence field in a small wind tunnel. Fluid Dyn Res 8(1-4):53

Melina G, Bruce PJK, Vassilicos JC (2016) Vortex shedding effects in grid-generated turbulence. Phys Rev Fluids 1(4):044402

Mohamed MS, Larue JC (1990) The decay power law in grid-generated turbulence. J Fluid Mech 219:195–214

Mora DO, Pladellorens EM, Turró PR, et al (2019) Energy cascades in active-grid-generated turbulent flows. Phys Rev Fluids 4(10):104601

Morikawa K, Urano S, Sanada T, et al (2008) Turbulence modulation induced by bubble swarm in oscillating-grid turbulence. J Power Energy Syst 2(1):330–339

Mydlarski L, Warhaft Z (1996) On the onset of high-Reynolds-number grid-generated wind tunnel turbulence. J Fluid Mech 320(1):331–368

Nagata K, Saiki T, Sakai Y, et al (2017) Effects of grid geometry on non-equilibrium dissipation in grid turbulence. Phys Fluids 29(1):015102

Nagata R, Watanabe T, Nagata K (2018) Turbulent/non-turbulent interfaces in temporally evolving compressible planar jets. Phys Fluids 30(10):105109

Namer I, Ötügen MV (1988) Velocity measurements in a plane turbulent air jet at moderate Reynolds numbers. Exp Fluids 6(6):387–399

Nichols JW, Lele SK, Ham FE, et al (2013) Crackle noise in heated supersonic jets. J Eng Gas Turbines Power 135(5):051202

Nieuwstadt JF. T .and Westerweel, Boersma B (2016) Introduction to Theory and Applications of Turbulent Flows. Springer

Ozono S, Ikeda H (2018) Realization of both high-intensity and large-scale turbulence using a multi-fan wind tunnel. Exp Fluids 59(12):1–12

Pack DC (1950) A note on Prandtl's formula for the wave-length of a supersonic gas jet. Quart J Mech Appl Math 3(2):173–181

Papamoschou D, Roshko A (1988) The compressible turbulent shear layer: an experimental study. J Fluid Mech 197:453–477

Pérez-Alvarado A, Mydlarski L, Gaskin S (2016) Effect of the driving algorithm on the turbulence generated by a random jet array. Exp Fluids 57(2):20

Pham TD, Watanabe T, Nagata K (2023) Large-eddy simulation of a flow generated by a piston-driven synthetic jet actuator. CFD Lett 15(8):1–18

Pizzaia A, Rossmann T (2018) Effect of boundary layer thickness on transverse sonic jet mixing in a supersonic turbulent crossflow. Phys Fluids 30(11)

Pope SB (2000) Turbulent Flows. Cambridge Univ. Pr.

Puga AJ, LaRue JC (2017) Normalized dissipation rate in a moderate Taylor Reynolds number flow. J Fluid Mech 818:184–204

Ristorcelli JR, Blaisdell GA (1997) Consistent initial conditions for the DNS of compressible turbulence. Phys Fluids 9(1):4–6

Saddoughi SG, Veeravalli SV (1994) Local isotropy in turbulent boundary layers at high Reynolds number. J Fluid Mech 268:333–372

Sakakibara H, Watanabe T, Nagata K (2018) Supersonic piston synthetic jets with single/multiple orifice. Exp Fluids 59(5):76

Sreenivasan KR, Antonia RA (1997) The phenomenology of small-scale turbulence. Annu Rev Fluid Mech 29(1):435–472

Suzuki H, Nagata K, Sakai Y, et al (2010) High-Schmidt-number scalar transfer in regular and fractal grid turbulence. Phys Scr 2010(T142):014069

Takamure K, Ozono S (2019) Relative importance of initial conditions on outflows from multiple fans. Phys Rev E 99(1):013112

Tam CKW (1972) On the noise of a nearly ideally expanded supersonic jet. J Fluid Mech 51(1):69–95

Tan HS, Ling SC (1963) Final stage decay of grid-produced turbulence. Phys Fluids 6(12):1693–1699

Tan S, Xu X, Qi Y, et al (2023) Scalings and decay of homogeneous, nearly isotropic turbulence behind a jet array. Phys Rev Fluids 8(2):024603

Theunissen R (2010) Adaptive image interrogation for PIV: Application to compressible flows and interfaces. PhD thesis, TU Delft, Delft University of Technology, Delft, The Netherlands

Thormann A, Meneveau C (2014) Decay of homogeneous, nearly isotropic turbulence behind active fractal grids. Phys Fluids 26(2)

Traub LW, Sweet M, Nilssen K (2012) Evaluation and characterization of a lateral synthetic jet actuator. J Aircraft 49(4):1039–1050

Uberoi MS, Wallis S (1967) Effect of grid geometry on turbulence decay. Phys Fluids 10:1216–1224

Valente PC, Vassilicos JC (2011) The decay of turbulence generated by a class of multiscale grids. J Fluid Mech 687:300–340

Valente PC, Vassilicos JC (2014) The non-equilibrium region of grid-generated decaying turbulence. J Fluid Mech 744:5–37

Valente PC, Onishi R, da Silva CB (2014) Origin of the imbalance between energy cascade and dissipation in turbulence. Phys Rev E 90(2):023003

Variano EA, Bodenschatz E, Cowen EA (2004) A random synthetic jet array driven turbulence tank. Exp Fluids 37(4):613–615

Vassilicos JC (2015) Dissipation in turbulent flows. Annu Rev Fluid Mech 47:95–114

Wang M, Yurikusa T, Sakai Y, et al (2022) Interscale transfer of turbulent energy in grid-generated turbulence with low Reynolds numbers. Int J Heat Fluid Flow 97:109031

Watanabe T, Nagata K (2023) The response of small-scale shear layers to perturbations in turbulence. J Fluid Mech 963:A31

Watanabe T, Sakai Y, Nagata K, et al (2016) Large eddy simulation study of turbulent kinetic energy and scalar variance budgets and turbulent/non-turbulent interface in planar jets. Fluid Dyn Res 48(2):021407

Watanabe T, Zhang X, Nagata K (2019) Direct numerical simulation of incompressible turbulent boundary layers and planar jets at high Reynolds numbers initialized with implicit large eddy simulation. Comput Fluids 194:104314

Watanabe T, Tanaka K, Nagata K (2021) Solenoidal linear forcing for compressible, statistically steady, homogeneous isotropic turbulence with reduced turbulent mach number oscillation. Phys Fluids 33(9):095108

Westerweel J, Scarano F (2005) Universal outlier detection for PIV data. Exp Fluids 39(6):1096–1100

Williams JEF, Simson J, Virchis VJ (1975) 'crackle': An annoying component of jet noise. J Fluid Mech 71(2):251–271

Yamamoto K, Ishida T, Watanabe T, et al (2022a) Experimental and numerical investigation of compressibility effects on velocity derivative flatness in turbulence. Phys Fluids 34(5)

Yamamoto K, Watanabe T, Nagata K (2022b) Turbulence generated by an array of opposed piston-driven synthetic jet actuators. Exp Fluids 63(1):1–17

Zheng Y, Nagata K, Watanabe T (2021a) Energy dissipation and enstrophy production/destruction at very low Reynolds numbers in the final stage of the transition period of decay in grid turbulence. Phys Fluids 33(3):035147

Zheng Y, Nagata K, Watanabe T (2021b) Turbulent characteristics and energy transfer in the far field of active-grid turbulence. Phys Fluids 33(11):115119

Zhou Y, Nagata K, Sakai Y, et al (2018) Dual-plane turbulent jets and their non-gaussian velocity fluctuations. Phys Rev Fluids 3(12):124604

Zwart PJ, Budwig R, Tavoularis S (1997) Grid turbulence in compressible flow. Exp Fluids 23(6):520–522